ACS OMEGA

http://pubs.acs.org/journal/acsodf

Article

Fabrication of Graphene-Based TiO_2@CeO_2 and CeO_2@TiO_2 Core−Shell Heterostructures for Enhanced Photocatalytic Activity and Cytotoxicity

Mitra Malekkiani, Fatemeh Ravari,* Abbas Heshmati Jannat Magham, Mehdi Dadmehr, Heiko Groiss, Hasan Ali Hosseini, and Reza Sharif

Cite This: *ACS Omega* 2022, 7, 30601−30621

Read Online

ACCESS | Metrics & More | Article Recommendations | Supporting Information

ABSTRACT: Development of light-harvesting properties and inhibition of photogenerated charge carrier recombination are of paramount significance in the photocatalytic process. In the present work, we described the synthesis of core−shell heterostructures, which are composed of titanium oxide (TiO_2) and cerium oxide (CeO_2) deposited on a reduced graphene oxide (rGO) surface as a conductive substrate. Following the synthesis of ternary rGO-CeO_2@TiO_2 and rGO-TiO_2@CeO_2 nanostructures, their photocatalytic activity was investigated toward the degradation of rhodamine B dye as an organic pollutant under UV light irradiation. The obtained structures were characterized with high-resolution transmission electron microscopy, field-emission scanning electron microscopy, energy-dispersive X-ray spectroscopy, Fourier transform infrared spectroscopy, X-ray diffraction, Brunauer−Emmett−Teller, X-ray photoelectron spectroscopy surface analysis, and UV−Vis spectroscopy. Various parameters including pH, catalyst dosage, temperature, and contact time were studied for photocatalysis optimization. Heterostructures showed considerable advantages because of their high surface area and superior photocatalytic performance. In contrast, rGO-CeO_2@TiO_2 showed the highest photocatalytic activity, which is attributed to the more effective electron−hole separation and quick suppression of charge recombination at core−shell phases. A biological assay of the prepared heterostructure was performed to determine the cytotoxicity against breast cancer cells (MCF-7) and demonstrated a very low survival rate at 7.65% of cells at the 17.5 mg mL^{-1} concentration of applied photocatalyst.

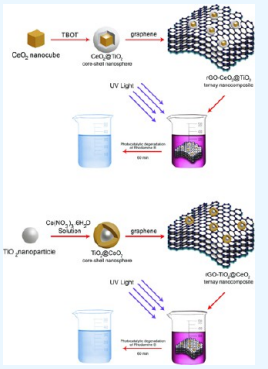

1. INTRODUCTION

The presence of organic pollutants in water reservoirs is regarded as one of the most critical environmental problems that impact the natural ecological systems through growth inhibition of living organisms and creatures in water. Also, water pollution is the determining factor for human beings' safety. Among the pollutants in wastewater, organic materials are the most common agents released during industrial processes.[1] The accumulation of industrial organic compounds in water reservoirs would harm the aquatic ecosystem.[2] Dye wastes are indicated as one of the most important pollutants that can be observed easily by the human eye and are resistant against natural decomposition.[3] Dyes are extremely stable agents during oxidation reactions and light exposure because of their complicated aromatic molecular structures.[4−6] Thus, treating wastewater, particularly removing their organic contaminants, is assumed as one of the most challenges in the wastewater refining process.[2] Diverse methods of wastewater refining for dye removal contain biological, chemical, and physical procedures like using selective filters, chemical coagulation, nonaerobic treatment, flotation, membrane separation, and electrochemical coagulation, which have been applied recently.[7] However, the major drawbacks of these methods are high operational expenditures, creation of poisonous byproducts, technical limitations, ineffective dye decomposition, and low reported sensitivity to a variable wastewater flow. Another problem is the presence of one or more benzene rings in the chemical structure of dye compounds that are not easily degradable in biological and chemical processes. Furthermore, most of the dyes are resistant to standard treatment methods. One of the applied methods in advanced oxidation processes is photocatalysis, which is assumed as an effective and ecologically friendly approach in the environmental pollution control field.[8] Photocatalysis is referred as the green technology that presents several advantages such as facile construction,[9] low energy consumption,[10] handling of reacting conditions,[11] and absence of secondary pollution.[12] The photocatalytic procedure can be performed under visible light or/and UV light irradiation.[2] It has been reported that semiconductor-based catalysts have been considered for photocatalytic degradation of organic dyes in

Received: July 9, 2022
Accepted: August 4, 2022
Published: August 16, 2022

water treatment procedures.[13−16] Because of the photocatalytic activity of semiconductors, the absorbed light with higher energy than the semiconductor band gap will result in the generation of electron−hole pairs.[17] The generated holes and electrons can accelerate redox reactions, which results in the destruction of organic compounds in wastewater.[18,19] Various semiconductor-based photocatalysts are being applied to treat the wastewater contaminants. The most frequently applied semiconductors include ZnO, TiO_2, CeO_2, Ag_3PO_4, CdS, and so on,[20] which are considered as visible or UV light photocatalysts for oxidation of water molecules and photodecomposition of organic compounds.[2] Among them, TiO_2 has been extensively applied in photocatalytic structures because of its intrinsic features like high efficiency, chemical stability, low cost, and nontoxicity.[21,22] Nevertheless, the practical application of photocatalytic technology is greatly limited because of the low quantum effectiveness and the wide band gap (3.2 eV) of TiO_2.[23,24] The development of photocatalytic activity of TiO_2 has been considered in many studies through different strategies including integration with metal ions[25] or organic compounds,[26] tailoring morphology,[27] and formation of nanocomposites.[28] Therefore, one of the useful strategies to overcome TiO_2 deficiencies includes coupling TiO_2 with other narrow-band gap semiconductors for improving the absorption of visible light.[29] The integration of TiO_2 with several metal oxides such as SnO_2−TiO_2, ZrO_2−TiO_2, ZnO−TiO_2, Bi_2O_3−TiO_2, WO_3−TiO_2, Cu_2O−TiO_2, CeO_2−TiO_2, and In_2O_3−TiO_2 has improved the activity of applied photocatalysts.[30−36] The synthesized heterogeneous nanocomposites showed a remarkable function and performance compared with applied TiO_2 NPs alone. The remarkable properties of these nanocomposites would be broad visible light absorption, long charge carrier lifespan, and high rate of charge separation and transfer.[37] Among different inorganic oxide catalysts, CeO_2 has been considered in many studies because of its great thermal constancy, easy transition between Ce(IV) and Ce(III) oxidation states, high UV absorption ability, and enhanced electrical conductivity. Particularly, the oxygen released by CeO_2 as an oxygen carrier plays a crucial role in oxidation reactions.[38,39] Coupling TiO_2 with CeO_2 could enhance the separation of electron−hole pairs and the photocatalytic activity.[40] Many core−shell-based structures have been fabricated recently as photocatalysts, which are composed of two or three composited semiconductors because they could create multiple interfaces in order to increase their functional properties.[41] Li et al. prepared an α-Fe_3O_4@TiO_2 microstructure through a controlled coating process, which showed superior photocatalytic activity toward degradation of rhodamine B (RhB) dye.[42] Ye et al., synthesized Fe_3O_4/SiO_2/TiO_2 composite with a core−shell structure, which showed higher RhB dye degradation in comparison with TiO_2 NPs as well as Fe_3O_4/SiO_2 structures.[43] The observed enhanced photocatalytic activity of photocatalysts with a core−shell structure is commonly attributed to the created photoinduced electron−hole through the formation of heterojunction interfaces in the core−shell structures.[44] Another efficient strategy to improve the function of the semiconductor photocatalyst involves the application of carbon substances in the composite, which displays an efficient electron transfer substrate. For this purpose, two-dimensional carbon substances such as activated carbon, graphene oxide (GO), graphene, and graphdiyne have been applied in the semiconductor photocatalytic structure.[45] Graphene has recently attracted much attention because of its intrinsic high electrical conductivity, large surface area, superior mechanical features, excellent optical transparency, great thermal/chemical stability,[46] and also their capability of anchoring molecules on its base planes through guest−host interaction.[45] Graphene is a one-layer sheet of sp^2-hybridized carbon atoms in a lattice that resembles a two-dimensioned honeycomb.[47] Previous studies have illustrated that combining mineral materials with graphene improved their photocatalytic activities.[48] Thus, the integration of core−shell structures with graphene would enhance the performance of organic pollutant degradation and result in the increment of the photocatalytic properties. There are several reports on different biological applications of nanomaterials.[49−53] Among the different biological assays, cell cytotoxicity would be a crucial and determining factor for synthesized nanostructures, which was also discussed in the previous studies.[54] In the present study, we constructed an effective and low-cost photocatalyst for RhB degradation. The nanosized TiO_2 and CeO_2 powders were synthesized to prepare the TiO_2@CeO_2 and CeO_2@TiO_2 core−shell structures. To lower the recombination rate of photogenerated electrons and hole pairs, the core−shell structures were deposited on the graphene surface via aminopropyltriethoxysilane. Morphology and features of synthesized nanocomposite photocatalysts were determined by field-emission scanning electron microscopy (FESEM), high-resolution transmission electron microscopy (HRTEM), energy-dispersive X-ray spectroscopy (EDS), X-ray diffraction (XRD), X-ray photoelectron spectroscopy (XPS), Fourier transform infrared (FT-IR) spectroscopy, UV−Vis spectroscopy, and Brunauer−Emmett−Teller (BET) analysis. The photocatalytic performance of applied nanocomposites was assayed for removal and adsorption of RhB dye under the irradiation of UV light. Optimization of the RhB degradation experiment was conducted using some factors, such as the dosage of catalysts, the concentration of dye, temperature, and solution pH. Biological assay of experiment was performed through the determination of cell toxicity of the superior photocatalyst in the MCF-7 cell line.

2. EXPERIMENTAL SECTION

2.1. Materials and Chemical Agents. To prepare the applied solution, deionized water was used throughout the experiment. Tetrabutyltitanate (TBOT, $C_6H_{36}O_4Ti$; 99%), hydrazine hydrate ($N_2H_4{\cdot}H_2O$; 50%), ammonia (NH_3; 28%), ammonium bicarbonate (NH_4HCO_3; 99%), and cerium(III) nitrate hexahydrate ($Ce(NO_3)_3{\cdot}6H_2O$; 99.99%) were bought from Sigma-Aldrich, Germany. Graphite powders (99.5%), ethanol (C_2H_5OH; 99.5%), sulfuric acid (H_2SO_4; 98%), sodium nitrate ($NaNO_3$; 99%), potassium permanganate ($KMnO_4$; 98.5%), hydrogen peroxide (H_2O_2; 30%), sodium hydroxide (NaOH; 99%), hydrochloric acid (HCl; 30%), and 3-aminopropyltriethoxysilane (APTES; 98%), were purchased from Merck. Other chemicals used in the experiments had analytical-purity grades without further purification.

2.2. Characterization Techniques. Spectroscopy analysis and determination of optical bandgaps of synthesized photocatalysts were performed using a UV−Vis spectrophotometer (Shimadzu, Japan) to optimize the conditions of the photocatalytic degradation and photocatalytic degradation. A hotplate stirrer was used to stir solutions to conduct the photocatalytic experiments under an 11 W UV-A lamp. Sonication was performed with a Hielscher ultrasonic processor (50 kHz, 200

https://doi.org/10.1021/acsomega.2c04338
ACS Omega 2022, 7, 30601−30621

W, UTR200, Germany) equipped with a titanium probe with 10 mm diameter, which was applied to homogenize the solution.

The physical as well as morphological features of the synthesized photocatalysts were ascertained using diverse characterization techniques. To obtain the XRD pattern and crystalline nature of nanostructures, a Philips analytical diffractometer was applied. The FT-IR analysis was performed by FT-IR spectroscopy (Shimadzu 8400, Japan). X-ray spectroscopy (EDX Tescan Brno-Mira Lmu), field-emission scanning electron microscopy (FESEM energy-dispersive), and TEM (JEM-2200FS, JEOL, Japan) equipped with an Oxford Instruments X-Max^N 80 T EDS-detector, at 200 keV primary beam energy were used to identify the morphology and size of the synthesized nanomaterial. The instrument was operated in conventional TEM mode, using a TemCam-XF416 (TVIPS, Germany), and scanning mode (STEM), using a bright field (BF) and a high-angle annular dark field detector. For sample preparation, the nanocrystals were dispersed in ultrapure water in an ultrasonic bath for 20 min, dropped on holey-carbon TEM grids, and dried under vacuum conditions for 1 day. XPS analysis was performed using a Thermofisher Theta Probe XPS system, and the Avantage software package was utilized for assessment of obtained spectra. A monochromatic Al Kα X-ray source (1486.6 eV) with a spot size of 400 μm and a power of 100 W was used for irradiation of samples. For access to high-resolution spectra, a pass energy of 20 eV and an energy step size of 0.05 eV were used. Standard charge shift reference of the spectra was performed through a peak of adventitious carbon at 285.0 eV. The C 1s and O 1s photoelectron peaks with linear or Shirley background subtraction and normalization using Scofield sensitivity factors were used for qualitative and quantitative analyses of obtained results. For measurement of the nanomaterial BET surface, a BET belsorp mini II tool was applied using the nitrogen physical adsorption at 100 and 300 °C before performing experiments, and finally, the nanomaterials were degassed for 4 h.

2.3. Synthesis of TiO_2 Nanoparticles. A simple sol-hydrothermal-based procedure was used to achieve the anatase TiO_2 nanoparticles. TBOT was applied as the titanium source. At first, 4 mL of TBOT was added to 60 mL of ethanol under continuous stirring at ambient temperature. Later on, 80 mL of deionized water was added to the solution dropwise under strenuous stirring. As a result, a white solution mixture was obtained while being stirred continuously for 30 min. In the next stage, the acquired mixture along with 2.0 g of ammonium bicarbonate was moved into a 200 mL Teflon-linear steel autoclave and kept at 160 °C for 12 h, and later it was cooled at ambient temperature. The obtained precipitate was ultimately rinsed with deionized water and dehydrated alcohol. Then, the obtained precipitate was dried at 50 °C for 12 h. Ultimately, it was collected and utilized for more investigation.[55]

2.4. Synthesis of CeO_2 Nanocubes. A hydrothermal method was applied for the synthesis of CeO_2 nanocubes as mentioned before.[56] 10 mL of $Ce(NO_3)_3{\cdot}6H_2O$ (4 mM) and 70 mL of NaOH (480 mM) were prepared in deionized water. Then, the $Ce(NO_3)_3$ solution was added drop by drop to the solution of NaOH, and the suspension was stirred for 30 min at room temperature so that a pale purple solution was obtained. Then, the mixture transferred to a Teflon-lined stainless-steel autoclave, and it was heated up to 180 °C for 24 h. The obtained CeO_2 nanocubes were centrifuged and washed with deionized water several times until the pH became neutral, and afterward, they were washed many times using ethanol. The product was then dried for 24 h at 80 °C under vacuum conditions and later calcined in an air atmosphere at 600 °C for 5 h to obtain the yellow CeO_2 nanocubes.

2.5. Synthesis of CeO_2@TiO_2 Core−Shell Nanospheres. The CeO_2@TiO_2 core−shell was synthesized according to the Stober method.[56] TBOT served as the TiO_2 precursor for synthesis of the CeO_2@TiO_2 shell. Briefly, 0.075 g of CeO_2 nanocubes were added to 100 mL of absolute ethanol, and then it was dispersed and mixed with the concentrated ammonia solution (0.30 mL, 28%) by ultrasonication for 20 min. Then, TBOT (0.75 mL) was added dropwise for 2 min, and then the mixture was stirred at 45 °C for 24 h. Then, the obtained mixture was centrifuged, and the precipitate was rinsed with deionized water and ethanol three times. The synthesized powder was dehydrated at 100 °C overnight and then calcined at 500 °C for 2 h in air so that its organic species were removed.

2.6. Synthesis of TiO_2@CeO_2 Core−Shell Nanospheres. In a typical process, using a facile hydrothermal method, the TiO_2@CeO_2 core−shell was synthesized. To achieve this purpose, in the beginning, 0.035 g TiO_2 nanoparticles were added to 35 mL of NaOH (480 mmol). Following, 0.912 g $Ce(NO_3)_3{\cdot}6H_2O$ was dissolved in 10 mL of deionized water. Then, the $Ce(NO_3)_3$ solution was added drop by drop to the NaOH solution for 2 min and stirred for 30 min at ambient temperature. The obtained solution was carried over to a 100 mL Teflon-lined stainless-steel autoclave and then heated for 24 h at 180 °C so that the TiO_2@CeO_2 core−shell was acquired. After centrifugation, the product was washed using deionized water so that the pH became neutral, and afterward, it was washed three times with ethanol. The precipitate was then dried for 24 h at 80 °C under vacuum conditions, and later it was calcined for 5 h at 600 °C in air to prepare the TiO_2@CeO_2 core−shell nanosphere.

2.7. Synthesis of Reduced GO (rGO). According to the Hummers method, GO was synthesized from graphite flakes.[57] In the initial step, a mixture including 3 g of graphite and 1.5 g of $NaNO_3$ was added to 69 mL of H_2SO_4. The temperature of the obtained solution was then cooled down to 0 °C using an ice bath while stirring for 1 h. Then, 3 g of $KMnO_4$ was precisely mixed with the above solution to retain the reaction temperature below 20 °C. Following, the solution mixture was stirred for 30 min at 35 °C and then, 138 mL of ultrapure deionized water was slowly added, so that the amount of exothermic heat was generated that increased the temperature to 98 °C. The temperature was kept constant for 15 min, and then 420 mL of warm water was added to create another exotherm condition, followed by slowly adding 10 mL of H_2O_2 (30%). The obtained solution was centrifuged and washed with HCl (5%) and deionized water to purify the mixture. The obtained solid material was dried at 65 °C under vacuum to obtain graphite oxide. After that, 1 g of graphite oxide was added to 2000 mL of deionized water in a round-bottom flask to obtain a heterogeneous yellow-brown solution. This solution was sonicated for 1 h to become a homogeneous solution. Then, 10.5 mL of hydrazine hydrate (50%) and 14.2 mL of NH_3 (25%) were added to the solution of 2000 mL of GO to prepare the rGO. In the next step, using refluxing the mixture for 24 h in an oil bath of 98 °C, GO nanosheets were reduced to graphene. This product was separated using centrifugation, and then it was washed with deionized water and ultimately dried at room temperature.[57]

2.8. Synthesis of rGO-NH_2. For amine functionalization of rGO, 100 mg of rGO was added to 100 mL of ethanol in a round-

https://doi.org/10.1021/acsomega.2c04338
ACS Omega 2022, 7, 30601−30621

bottom flask. Then, 200 μL of APTES was added dropwise to the solution mixture as mentioned above under constant stirring. Subsequently, the mixture was refluxed at 80 °C for 12 h, and then it was cooled to ambient temperature. The surface-functionalized material (rGO-NH_2) was then collected by centrifugation and finally washed with ethanol.[58]

2.9. Synthesis of rGO-CeO_2@TiO_2 and rGO-TiO_2@CeO_2. TiO_2@CeO_2 and CeO_2@TiO_2 (10 Mm, 1 mL) solutions were added to the above rGO-NH_2 suspension separately with the same procedure. The reaction solution mixture was reacted for 6 h. Then, it was heated at 80 °C for 2 h, and then it was cooled to ambient temperature. The prepared products, rGO-CeO_2@TiO_2 and rGO-TiO_2@CeO_2, were collected by centrifugation and washed with ethanol.[58]

2.10. Photocatalytic Activity Measurements. To evaluate the photocatalytic performance of the as-prepared photocatalyst, the degradation of RhB was assessed using UV light irradiation. For optimization of the photocatalytic process, some parameters were assayed, which include the degradation time, pH effect, temperature effect, and concentration of the photocatalyst. After the optimization process, a small amount of the photocatalyst (30 mg) was dispersed in 100 mL of RhB aqueous solution (3 mg L^{-1}) under 298 K temperature and pH 9 condition. Then the solution was stirred for 30 min in darkness, and the adsorption/desorption equilibrium was attained. In the next step, the photocatalytic activity was achieved by an 11 W UV lamp, while the distance between the beaker base and UV light source was 20 cm. This test was performed under UV light for 180 min, and the solution aliquots (3 mL) were taken out every 20 min during the test, and later they were centrifuged in order to remove the particles of the photocatalyst. In each aliquot, the RhB concentration was determined using a UV−Vis spectrometer at the 554 nm absorption wavelength. The percentage of the RhB degradation rate was measured using eq 1.

$$\text{Dye degradation (\%)} = \frac{C_0 - C_t}{C_t} \times 100 \quad (1)$$

where C_0 and C_t represent the initial and the residual pollutant concentration before and after UV light irradiation, respectively. To fit the experimental data, the first-order kinetic equation (eq 2) was applied.

$$\ln\left(\frac{C_0}{C}\right) = k_{app} \times t \quad (2)$$

In the abovementioned equation, k_{app} is the reaction rate constant and t is the reaction time.

2.11. Adsorption Tests. In the same way, the adsorption ability of photocatalysts was determined by the adsorption experiments of RhB in darkness. In this experiment, 30 mg of catalyst was added to 100 mL of RhB solution with the same concentration under the specific condition including 298 K and pH 9. The solution was stirred for another 30 min under dark conditions to achieve the absorption−desorption equilibrium. Then, 5 mL of sample were taken out every 20 min intervals regularly and centrifuged to separate the catalysts. Finally, the absorbance values of samples at the wavelength of λ_{max} = 554 nm were recorded using a UV−Vis spectrophotometer.

2.12. 3-(4,5-Dimethylthiazol-2-yl)-2,5-diphenyltetrazolium Bromide (MTT) Assay. To determine the toxicity of the applied photocatalyst, we performed the cell toxicity experiment by MTT assay. The MCF-7 cell line was prepared from the Iranian Biological Resource Center (IBRC C10082, IBRC, Tehran, Iran) and cultured in DMEM/F12 medium supplemented with 10% fetal bovine serum (FBS) and 1% penicillin/streptomycin. In the present experiment, MTT analysis was used to determine the cell viability; 10,000 cells per each well were incubated in 96-well plates containing 100 μL of 5% FBS and then incubation at 37 °C for 48 h. After incubation for 48 h, different concentrations of applied photocatalyst were added to the wells and incubated for another 48 h. Afterward, 59 μL of MTT (5 mg mL^{-1}) was added to each well and incubated for another 5 h. Then 110 μL of dimethyl sulfoxide was used to solubilize the generated formazan crystals, and the absorbance at 570 nm was recorded through a microplate reader to determine the cell viability. The cell viability was determined according to the cell viability = A of treated cells/A of control sample cells × 100. The assay results were expressed as the mean ± SD of triplicates.

3. RESULTS AND DISCUSSION

3.1. Structural and Morphological Features of Prepared Nanostructures. To evaluate the catalyst's effectiveness, morphology plays a crucial role. The morphology and structure of nanostructures were tested using FESEM and HRTEM. Figure 1 represents the images that are attained employing FESEM of nanoparticles, core−shell nanospheres, and ternary nanocomposites of (a) TiO_2, (b) CeO_2, (c) CeO_2@TiO_2, (d) TiO_2@CeO_2, (e) rGO-CeO_2@TiO_2, and (f) rGO-TiO_2@CeO_2. As shown in Figure 1a, TiO_2 nanoparticles have demonstrated a good structural uniformity while the edges and the grains are obviously spherical, and the TiO_2 nanoparticles showed uniform distribution without any agglomeration.[59,60] Moreover, it was measured that the TiO_2 nanoparticles have an average diameter of around 21.81 nm (Figure S1a). As presented in Figure 1b and S1b, the CeO_2 nanocubes had a smooth surface while an average size about 30.97 nm. Figure 1c shows that CeO_2 nanocubes after being coated with TiO_2 transformed to bigger and rougher NPs. The obtained results implied that CeO_2@TiO_2 core−shell nanospheres were formed with mean diameter about 35.74 nm (Figure S1c). In addition, Figure 1d showed that TiO_2 spherical nanoparticles after being wrapped in the cerium oxide shell and the TiO_2@CeO_2 core−shell nanospheres had still spherical form compared with TiO_2 spheres, but the obtained surface was rougher and textured because of the presence of CeO_2 nanoparticles deposited on the TiO_2 spheres. The mean TiO_2@CeO_2 core−shell nanosphere size was 27.93 nm (Figure S1d). Figure 1e,f clearly showed that after adding rGO, the CeO_2@TiO_2 and TiO_2@CeO_2 core−shell nanospheres were uniformly placed on the rGO sheets while there were ripples and wrinkles.[61] Thus, these consequences reveal further that rGO-CeO_2@TiO_2 and rGO-TiO_2@CeO_2 ternary nanocomposites were successfully synthesized. Additionally, the agglomeration procedure is usually reported when core−shell nanospheres are deposited on graphene sheets. The agglomeration of core−shell nanospheres may increase the photocatalytic efficiency because the recombination between photogenerated charge pairs was inhibited using the interparticle charge transfer induced in agglomerates.[62] To investigate the composition of rGO-CeO_2@TiO_2 and rGO-TiO_2@CeO_2 ternary nanocomposites, EDS was applied (Figure 1g−l). As illustrated in Figure 1i,j, all the spectrum elements, involving titanium (Ti), cerium (Ce), and oxygen (O), correspond to the core−shell nanospheres. Furthermore, Figure 1k,l shows the presence of Ti, Ce, O, and C,

https://doi.org/10.1021/acsomega.2c04338
ACS Omega 2022, 7, 30601−30621

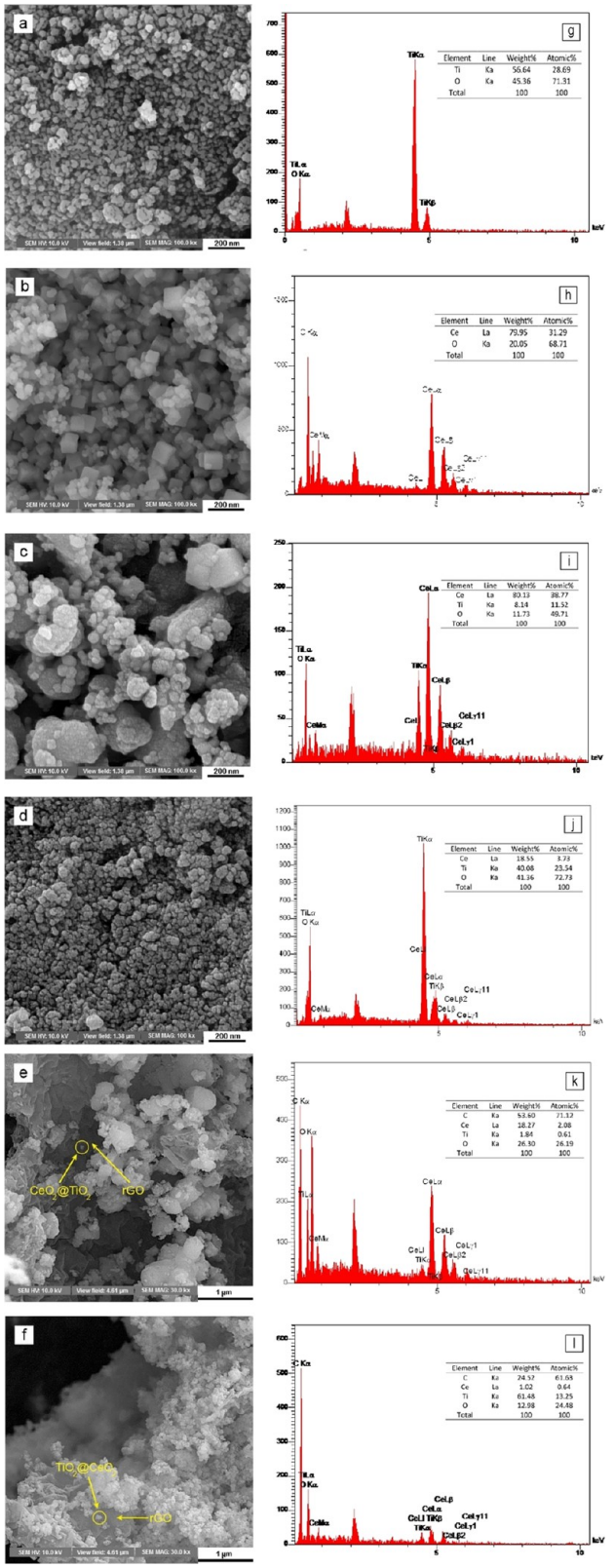

Figure 1. FESEM images of (a) TiO_2 nanoparticles, (b) CeO_2 nanoparticles, (c) CeO_2@TiO_2 core−shell nanospheres, (d) TiO_2@CeO_2 core−shell nanospheres, (e) rGO-CeO_2@TiO_2 ternary nanocomposites, and (f) rGO-TiO_2@CeO_2 ternary nanocomposites; EDS spectra of (g) TiO_2 nanoparticles, (h) CeO_2 nanoparticles, (i) CeO_2@TiO_2 core−shell nanospheres, (j) TiO_2@CeO_2 core−shell nanospheres, (k) rGO-CeO_2@TiO_2 ternary nanocomposites, and (l) rGO-TiO_2@CeO_2 ternary nanocomposites.

which clearly demonstrate successful formation of ternary nanocomposites.

The EDS elemental mapping of rGO-CeO_2@TiO_2 and rGO-TiO_2@CeO_2 ternary nanocomposites is shown in Figure 2a,b, which approves the coexistence of all elements in the ternary nanocomposites and also confirms the uniform spread of Ti, Ce, C, and O elements.

TEM results of the as-prepared TiO_2@CeO_2 and CeO_2@TiO_2 and core−shell nanospheres are presented in Figure 3. CeO_2@TiO_2 core−shell nanospheres with typical sizes are shown in the TEM image of Figure 3a, and an HRTEM image of a single nanosphere is presented in Figure 3b. HRTEM proved the formation of a core−shell structure and the sizes of the CeO_2 core and TiO_2 shell were 31 and 4.5 nm respectively. The marked interplanar '*d*' spacing of 0.36 nm of the CeO_2@TiO_2 structure corresponds to the (101) plane of the anatase TiO_2 shell, whereas the fringes of the core are not resolved in this projection of the structure. By scanning transmission electron microscopy (STEM) combined with EDS, we determined the elemental composition of another CeO_2@TiO_2 core−shell nanosphere. The recorded EDS map is shown in Figure 3c and displays the Ce and Ti distribution and confirms the nanosphere composition of a CeO_2 core and a TiO_2 shell. The TiO_2 is not evenly distributed, which could be induced by the facets of the nanocrystal core, which are well visible in Figure 3b. The reason could be either a simple geometric effect of a faceted core in a sphere-shaped shell or different growth kinetics on top the different facets. Figure 3d is a sum spectrum of the EDS map and shows clearly the Ce, Ti, and O peaks (as well as a C peak from the C-grid membrane). A quantitative analysis results in 49 at% O, 16 at% Ti and 35 at% Ce, pointing to a not fully oxidized structure. From the presented map in Figure 3c, a line scan was extracted, which is displayed in Figure 3e, and it approves the CeO_2 core and a thin layer of TiO_2 forming the shell structure. The concentration of Ti decreased toward the center of the nanocrystal but never reaches zero, a result of the geometrical projection of the core−shell structure by the measurement. On the basis of these results, we can conclude that the CeO_2@TiO_2 core−shell nanospheres had been accomplished.

The TEM results of the TiO_2@CeO_2 core−shell nanospheres are illustrated in Figure 3f−j. Again, an overview of the TiO_2@CeO_2 nanospheres shown in Figure 3f nanospheres with typical sizes and the HRTEM allows a view of the shape and crystallinity (Figure 3g). The diameter of the core was measured for this kind of crystal with 27 nm while the shell thickness was around 2.2 nm. The HRTEM image of the TiO_2@CeO_2 nanosphere depicts the lattice fringes of the shell at a *d*-spacing of 0.31 nm corresponding to the *d*-spacing of the (111) plane of CeO_2. Again, EDS was performed to analyze the presence of the different elements. The STEM-EDS elemental mapping (Figure 3h) of this sphere clearly indicates a well-defined, thickness-varying CeO_2 shell on a TiO_2 core, confirming the core−shell structure. The sum spectrum in Figure 3i represents the peaks of Ti, O, and Ce indicating the formation of TiO_2 and CeO_2. It is clearly visible that the different Ce and Ti peak size compared to Figure 3d, leading to a different quantification result of 57.5 at % O, 36.5 at % Ti and 6 at % Ce. This result fits well with the thinner shell thickness compared to the CeO_2@TiO_2 core−shell nanospheres, which can also be observed in the extracted line scan data of Figure 3j. The Ce ions were merely located in the shell region, and additionally, the Ti ions decreased strongly toward the surface. By observing all the above consequences, we could conclude the successful preparation of TiO_2@CeO_2

https://doi.org/10.1021/acsomega.2c04338
ACS Omega 2022, 7, 30601−30621

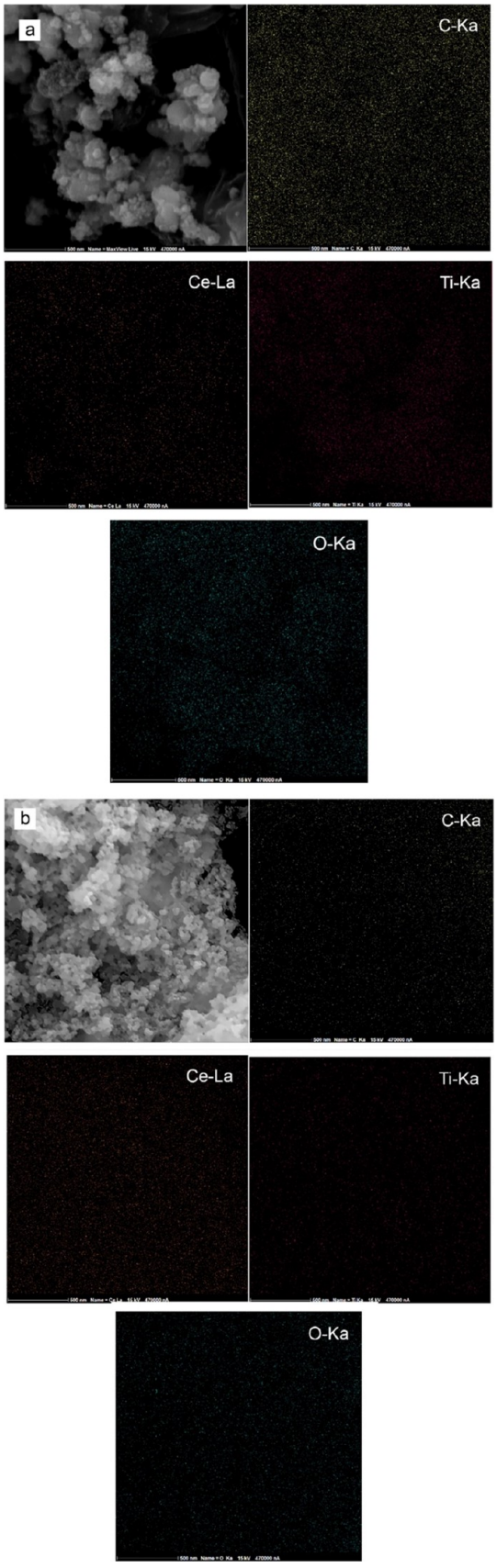

Figure 2. Elemental mapping of (a) rGO-CeO_2@TiO_2 ternary nanocomposites and (b) rGO-TiO_2@CeO_2 ternary nanocomposites.

core−shell nanospheres, and they confirmed the formation of a thin CeO_2 shell around the TiO_2 core.

3.1.1. FT-IR Analysis. FT-IR spectroscopy was performed to reveal the presence of the functional groups on the synthesized nanoparticles and nanocomposites. The FT-IR spectra for (a) TiO_2, (b) CeO_2, (c) rGO, (d) rGO-CeO_2@TiO_2, and (e) rGO-TiO_2@CeO_2 are shown in Figure 4. The bands at 1640 and 3400 cm^{-1} were attributed to bending vibration and O−H stretching and of the water molecules or the other substances containing hydroxyl groups.[46] A specific band was observed with wide absorption at the area with lower energy (<800 cm^{-1}) which illustrates the anatase O−Ti−O lattice. Generally, the obtained peaks lower than 600 cm^{-1} were attributed to metal oxide vibration and stretching modes. FT-IR spectra of pure CeO_2 in Figure 4b show a band at 505 cm^{-1} that corresponds to Ce−O vibration stretching mode.[63] According to Figure 4c, the GO peak decreased due to thermal exfoliations, and thus the peak of oxygen functional groups was completely reduced and totally removed. Thus, two wide peaks at 1562 and 1186 cm^{-1} were observed for the rGO. The peak at 1562 cm^{-1} can be attributed to the aromatic C═C stretch. The peak at 1186 cm^{-1} is related to the C−O stretch. This observation approved that the majority of oxygen functional groups in the GO were removed through thermal exfoliations in the synthesis conditions.[64] Figure 4d shows the FT-IR spectrum of the rGO-CeO_2@TiO_2 ternary nanocomposite while the absorption bands that were around 700 cm^{-1} correspond to the combination of Ti−O−Ti and Ti−O−C vibration, proposing that CeO_2@TiO_2 core−shell nanospheres have been bonded on the carbon layers of rGO chemically. The absorption band that appears at around 1600 cm^{-1} is due to the skeletal vibration of rGO sheets.[46] The spectrum of CeO_2@TiO_2 core−shell nanospheres in comparison with TiO_2 and CeO_2 was roughly identical to them. Moreover, a new broad band appears at about 505 cm^{-1}, which suggests that the scarce earth element Ce exists in the product in the form of an oxide.[40] As a result of the above facts, we can conclude that there is a coupling impact between the CeO_2@TiO_2 core−shell nanosphere and graphene. Additionally, in Figure 4e, the characteristic bands in rGO and the broad band were observed below 1000 cm^{-1}, which resulted from disappearance of the cerium band in the rGO-TiO_2@CeO_2 ternary nanocomposite due to the low amount or merging CeO_2 with the specific band of TiO_2.

3.1.2. XRD Analysis. To determine the crystal phase and structure nanomaterials, the XRD analysis has been performed. The XRD patterns of (a) CeO_2@TiO_2, (b) TiO_2@CeO_2, (c) rGO-CeO_2@TiO_2, and (d) rGO-TiO_2@CeO_2 are illustrated in Figure 5. Figure 5a,b represented the characterization of anatase state of TiO_2 nanoparticles via diffraction peaks at 25.38°, 38.02°, 48.10°, 55.7°, and 62.77° that correspond to (101), (004), (200), (105), and (211) diffraction planes, which in turn refer to JCPDS card NO. 21-1272.[65] In the attained spectrum, no extra peaks were seen showing that the TiO_2 anatase state was pure. Also, Figure 5a,b, represented that the diffraction feature peaks at (2θ) = 28.46°, 33°, 47.46°, 56.31°, 59.06°, and 69.06° corresponded with the face centered cubic structure of CeO_2 at (111), (200), (220), (311), (222), and (400) planes (JCPDS NO. 34-0394), respectively.[65] Thus, Figure 5a showed that almost all the diffraction peaks of CeO_2@TiO_2 core−shell nanospheres correspond with those of the TiO_2, whereas the diffraction peaks at 28.3° and 33° proved the existence of CeO_2. Because of the appearance of titanium dioxide peaks, the specific peak of cerium oxide was covered up. The impurity diffraction

https://doi.org/10.1021/acsomega.2c04338
ACS Omega 2022, 7, 30601−30621

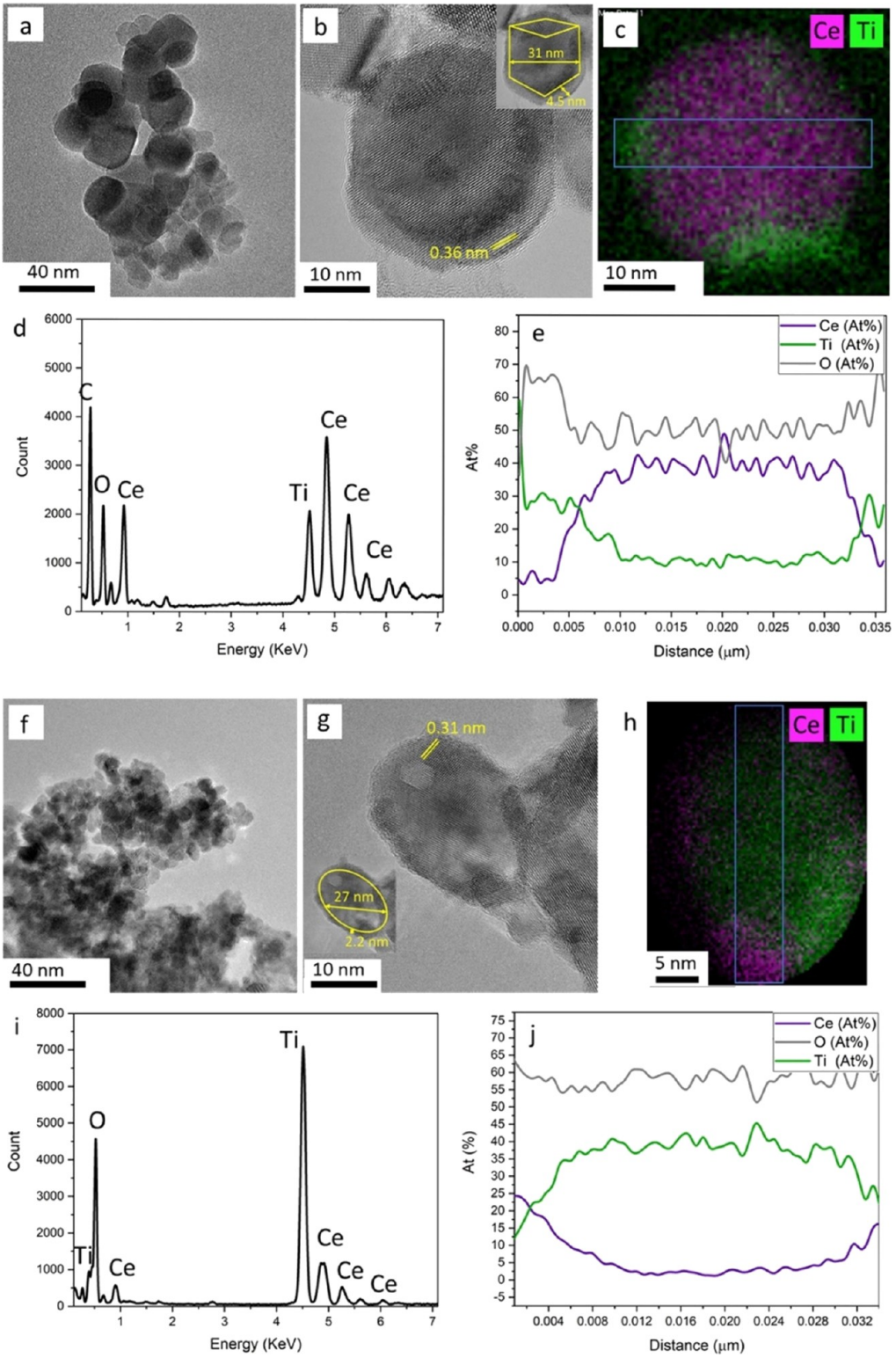

Figure 3. (a) TEM image of CeO_2@TiO_2 core−shell nanospheres, (b) HRTEM image of a CeO_2@TiO_2 core−shell nanosphere, (c) EDS map of a CeO_2@TiO_2 core−shell nanosphere, (d) sum spectrum of the CeO_2@TiO_2 nanosphere EDS map, (e) extracted line scan through the sphere, indicated by the blue rectangle in (c), (f) TEM image of TiO_2@CeO_2 core−shell nanospheres, (g) HRTEM image of a TiO_2@CeO_2 core−shell nanosphere, (h) EDS map of a TiO_2@CeO_2 core−shell nanosphere, (i) sum spectrum of the TiO_2@CeO_2 nanosphere EDS map, and (j) extracted line scan through the sphere, indicated by the blue rectangle in (h).

peaks were not found, implying that the product was highly pure. Based on Figure 5b, the diffraction peaks of the core−shell produced particles were in correspondence with the cubic structure of CeO_2 and anatase TiO_2, which indicated that TiO_2 nanoparticles were wrapped with the CeO_2 shell through the sol−gel hydrothermal method. Moreover, in this pattern no other diffractive peaks exist. The obtained observation suggested that the interface formation between TiO_2 and cubic CeO_2

https://doi.org/10.1021/acsomega.2c04338
ACS Omega 2022, 7, 30601−30621

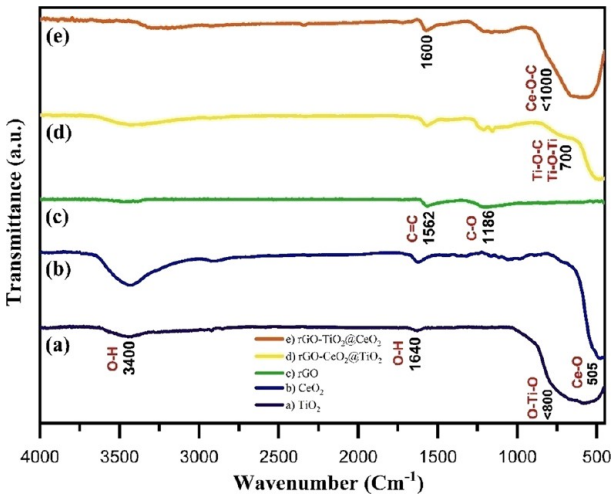

Figure 4. FT-IR spectra of (a) TiO_2 nanoparticles, (b) CeO_2 nanoparticles, (c) rGO, (d) rGO-CeO_2@TiO_2 ternary nanocomposites, and (e) rGO-TiO_2@CeO_2 ternary nanocomposites.

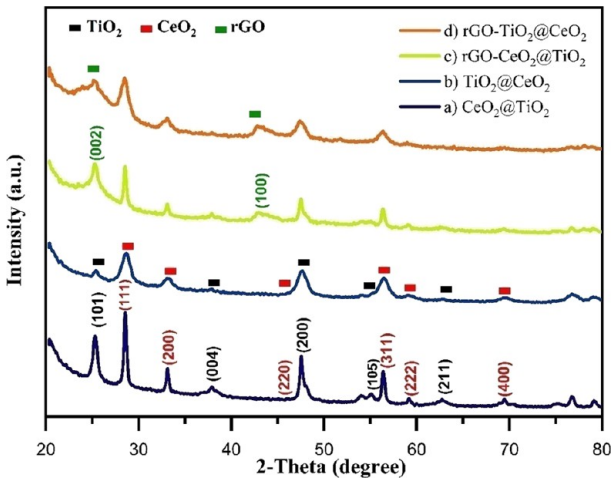

Figure 5. XRD patterns of (a) CeO_2@TiO_2 core–shell nanospheres, (b) TiO_2@CeO_2 core–shell nanospheres, (c) rGO-CeO_2@TiO_2 ternary nanocomposites, and (d) rGO-TiO_2@CeO_2 ternary nanocomposites.

becomes constant thermodynamically, and there was no new phase. As shown in Figure 5c, the XRD pattern of decreased GO (rGO) depicts a wide reflection at 24.7° that confirms few layer graphene sheets and a little concentrated peak around 44° which shows a turbostratic behavior of nonorderly carbon layers after removing the oxygen that includes functional groups,[66] and this corresponds to (002) and (100) crystal planes of rGO nanosheets. Nevertheless, the existence of graphene could not be differentiated using the XRD pattern of the ternary nanocomposites because the feature peak locality of the rGO (002) plane is very near to that of the (101) plane of anatase (at 25.38°), and the two peaks may overlap around 25° in the XRD background.[46]

In the XRD pattern, the ternary nanocomposite was identical to that of as-prepared pure TiO_2 and CeO_2. In the ternary nanocomposite, no other phases had been observed, which approves the purity of the synthesized substance. The mean crystalline size of nanocomposites was measured applying the formula of Scherrer,[48] and the obtained values were 8.17 and 6.85 nm for CeO_2@TiO_2 and TiO_2@CeO_2 structures, respectively. The crystal size of core–shell nanospheres was calculated and is shown in Table 1.

Table 1. Size Characterization of Core/Shell Samples

sample	2θ (°)	FWHM (rad)	diameter (nm)
CeO_2@TiO_2	25.2	0.0174	8.17
TiO_2@CeO_2	28.45	0.02	6.85

3.1.3. XPS Analysis. The chemical composition and oxidation mode of the elements were determined by XPS analysis. The survey scan from 0 to 1200 eV revealed all elements including Ti, Ce, O, and C of the CeO_2@TiO_2 and TiO_2@CeO_2 core–shell nanospheres in Figure 6a. Figure 6b–g showed XPS spectra of Ce 3d, Ti 2p, and O 1s, respectively. In Figure 6b,e, the Ce 3d spectra were fit with eight peaks, in which v and u represent the $3d_{5/2}$ and $3d_{3/2}$ spin orbitals, respectively. Eight peaks were determined at binding energies of 882.39, 883.59, 888.78, 889.25, 900.23, 904.14, 907.65, and 916.74 eV using the XPS curve fitting procedure. The above peaks are named v, v′, v″, v‴, u, u′, u″, and u‴ respectively. The precise scan of Ce $3d_{3/2}$ and Ce $3d_{5/2}$ modes are presented in Figure 6b,e, and also, the oxidative peaks are seen at 889.25 and 882.39 eV attributed to a satellite peak, which may originate from the spin-orbit coupling effect and resulted in separation or splitting of the energy level. The first oxidation peak is attributed to Ce $3d_{3/2}$ mode with a Ce $3d^9$ $4f^2$ O $2p^5$ ultimate state. The second oxidation peak is shown by Ce $3d^9$ $4f^1$ O $2p^6$ mode. Figure 6a,e depicts the oxidative Ce $3d_{5/2}$ peaks at 889.25 and 882.39 eV as features of the oxidation mode of Ce^{4+} ions, Ce $3d^9$ $4f^1$ O $2p^5$, and Ce $3d^9$ $4f^2$ O $2p^4$, respectively.[48] Figure 6c,f represents the oxidative state and chemical nature of Ti^{4+} ions. The oxidation peaks exhibited at 462 and 466.5 eV are related to the oxidation mode of binding energy for Ti $2p_{1/2}$ and Ti $2p_{3/2}$ representing that Ti^{4+} ions are present with octahedral oxygen coordination.[67] The O 1s spectra that are obtained for TiO_2@CeO_2 and CeO_2@TiO_2 and core–shell nanospheres are shown in Figure 6d,g, respectively. Both the major peaks were asymmetric, which showed the minimum existence of two types of oxygen on the surface. The fitted peak O_I at a BE of 531.5 eV indicated a surface oxygen lattice, namely, electron-bonded oxygen. Another observed peak O_{II} at a BE of 532.6 eV was attributed to chemically absorbed oxygen having the shape of $-OH/-CO_3^{2-}$ or adsorbed water.[56]

The atomic concentrations of TiO_2@CeO_2 and CeO_2@TiO_2 core–shell nanospheres are indicated in Table 2. The Ti atomic concentration on CeO_2@TiO_2 was 9.49%, which illustrated that the CeO_2 surface was covered with TiO_2, and the Ce atomic concentration on TiO_2@CeO_2 was 1.25%, which confirms the formation of TiO_2@CeO_2 core–shell nanospheres.

3.1.4. BET Analysis. The surface area and the pore diameter of used nanostructures are illustrated in the BET analysis. By applying N_2 adsorption–desorption measurements, the adsorption features of the synthesized nanostructures were investigated. Figure 7a–d display nitrogen adsorption–desorption isotherms of the synthesized CeO_2@TiO_2, TiO_2@CeO_2 core–shell nanospheres, and rGO-CeO_2@TiO_2, rGO-TiO_2@CeO_2 ternary nanocomposites. According to the obtained results, the data were measured by the BET equation and are displayed in Table 3. In comparison to the IUPAC classification, the entire adsorption–desorption isotherms displayed a type IV curve with H_3 hysteresis loops, confirming the presence of mesoporous with a mean diameter of 2–50 nm pore sizes. Based on Table 3, CeO_2@TiO_2 core–shell nanospheres have increased the area of

https://doi.org/10.1021/acsomega.2c04338
ACS Omega 2022, 7, 30601–30621

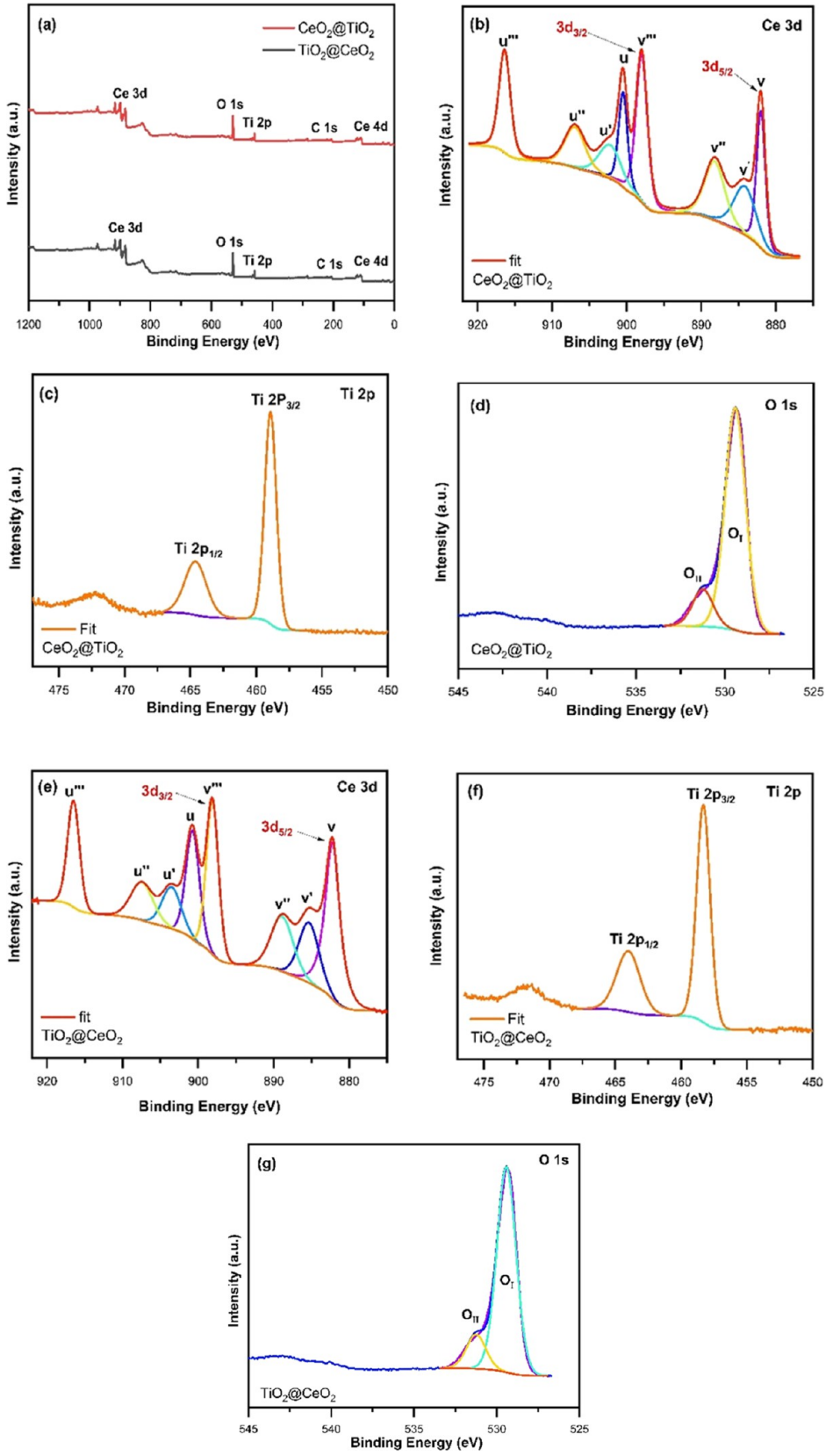

Figure 6. XPS analysis of the representative samples: (a) survey scan spectra of CeO_2@TiO_2 and TiO_2@CeO_2 core−shell nanospheres, (b) XPS Ce 3d data for CeO_2@TiO_2 core−shell nanospheres, (c) XPS Ti 2p data for CeO_2@TiO_2 core−shell nanospheres, (d) XPS O 1s data for CeO_2@TiO_2 core−shell nanospheres, (e) XPS Ce 3d data for TiO_2@CeO_2 core−shell nanospheres, (f) XPS Ti 2p data for TiO_2@CeO_2 core−shell nanospheres and, (g) XPS O 1s data for TiO_2@CeO_2 core−shell nanospheres.

https://doi.org/10.1021/acsomega.2c04338
ACS Omega 2022, 7, 30601−30621

Table 2. XPS Data of CeO_2@TiO_2 and TiO_2@CeO_2 Core−Shell Nanospheres

sample	peak	energy (eV)	peak width FWHM, (eV)	peak area (counts)	atomic (%)
CeO_2@TiO_2	Ti 2p	458.92	2.21	93894.3	9.49
	Ce 3d	882.34	2.73	37711.91	17.2
	O 1s	530.06	2.53	103295.6	67.67
	C 1s	284.71	1.97	13777.87	5.63
TiO_2@CeO_2	Ti 2p	458.9	2.23	24904.66	22.23
	Ce 3d	882.93	4.5	322039.6	1.25
	O 1s	529.96	2.51	76141.17	57.03
	C 1s	284.96	1.15	2473.15	19.49

the surface in small amounts in comparison to TiO_2@CeO_2 core−shell nanospheres, whereas rGO-CeO_2@TiO_2 and rGO-TiO_2@CeO_2 ternary nanocomposites showed a remarkable increase in the specific surface area.

The BET surface area of CeO_2@TiO_2, TiO_2@CeO_2, rGO-CeO_2@TiO_2, and rGO-TiO_2@CeO_2 was 20.456, 13.887, 55.375, and 54.876 m^2/g, respectively. The adsorption section of nitrogen isotherms and the Barrett−Joyner−Halenda procedure were used to calculate the corresponding pore size distribution patterns (Figure 7). The average pore diameter for

Table 3. Surface Area, Volume, and Pore Size Distribution of CeO_2@TiO_2 Core−Shell Nanospheres, TiO_2@CeO_2 Core−Shell Nanospheres, rGO-CeO_2@TiO_2 Ternary Nanocomposites, and rGO-TiO_2@CeO_2 Ternary Nanocomposites

samples	surface area BET (S_{BET}) (m^2/g)	pore size (nm) BJH_{ads}	total pore volume (P/P_0 = 0.990) (cm^3/g)
CeO_2@TiO_2	20.456	27.904	0.1427
TiO_2@CeO_2	13.887	26.194	0.0909
rGO-CeO_2@TiO_2	55.375	26.102	0.3614
rGO-TiO_2@CeO_2	54.876	23.901	0.3279

CeO_2@TiO_2, TiO_2@CeO_2, rGO-CeO_2@TiO_2, and rGO-TiO_2@CeO_2 was 27.904, 26.194, 26.102, and 23.901 nm, respectively. The obtained results have displayed an increasing amount of adsorbed N_2 after addition of rGO (up to 0.3614 and 0.3279 cm^3/g) from 0 to 0.9 for P/P_0 and showed great enhancement in pore volumes. Therefore, it was concluded that rGO-CeO_2@TiO_2 and rGO-TiO_2@CeO_2 had much larger pore volumes and surfaces than other samples and exhibited a high decrease in the pore diameter as compared with CeO_2@TiO_2 and TiO_2@CeO_2. The enhancement of the special surface area in ternary nanocomposites caused the possibility of enhancing the surface-active region and, in turn, resulted in the charge

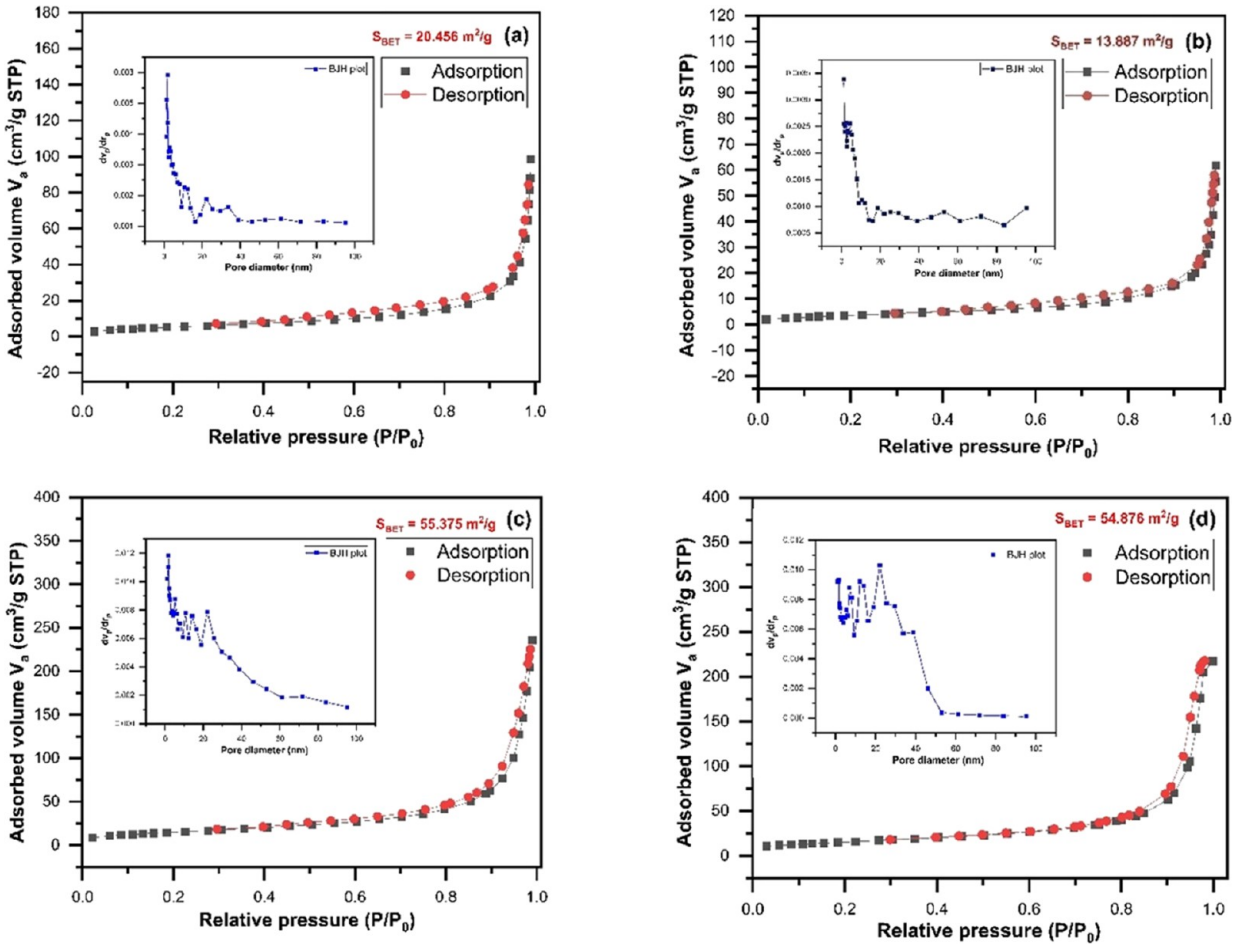

Figure 7. Nitrogen adsorption−desorption isotherms of (a) CeO_2@TiO_2 core−shell nanospheres, (b) TiO_2@CeO_2 core−shell nanospheres, (c) rGO-CeO_2@TiO_2 ternary nanocomposites, and (d) rGO-TiO_2@CeO_2 ternary nanocomposite, inset: pore size distribution of the prepared samples from the adsorption isotherm measurement.

https://doi.org/10.1021/acsomega.2c04338
ACS Omega 2022, 7, 30601−30621

transport. Also, the nanocomposite could enhance dye molecule degradation during the photocatalytic activity that results in a greater photocatalytic function in ternary nanocomposites. Not only enhancement in the surface area but also reduction in the pore size led to an increase in pore volume, which optimized the adsorption procedure by rGO-CeO_2@TiO_2 and rGO-TiO_2@CeO_2.

3.2. Electronic and Optical Features of the Samples. The UV−Vis diffuse reflectance spectra of (I) TiO_2, (II) CeO_2, (III) CeO_2@TiO_2, (IV) TiO_2@CeO_2, (V) rGO-CeO_2@TiO_2, and (VI) rGO-TiO_2@CeO_2 are plotted in Figure 8a. The band

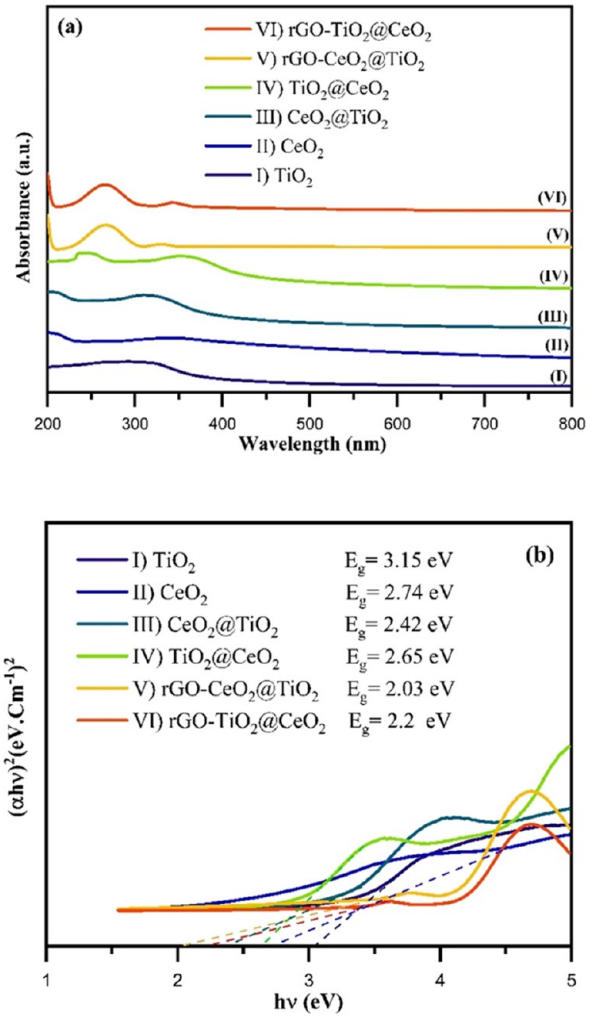

Figure 8. (a) UV−Vis diffuse reflecting spectra, (b) bandgap energies of (I) TiO_2, (II) CeO_2, (III) CeO_2@TiO_2 core−shell nanospheres, (IV) TiO_2@CeO_2 core−shell nanospheres, (V) rGO-CeO_2@TiO_2 ternary nanocomposites, and (VI) rGO-TiO_2@CeO_2 ternary nanocomposites.

gap edge of TiO_2 is around 400 nm. It shows the powerful light absorption of TiO_2 in the UV range, particularly at wavelengths that are lower than 400 nm. This would be because of the charge transfer in the material, especially from the transferred electrons from the valence band (VB) to conduction band (CB).[68] Also, the band gap edge of CeO_2 was around 500 nm. The CeO_2@TiO_2 core−shell nanospheres showed the redshift compared with TiO_2. This result is attributed to the cerium oxide that may absorb UV and visible light that could be caught by the TiO_2.[40] Therefore, it was concluded that deposition of the TiO_2 shell improved the light-harvesting effectiveness of CeO_2.[56] In addition, the adsorption edge of TiO_2@CeO_2 core−shell nanospheres was around 400 nm, and it showed a strong photoabsorption. Figure 8a (V and VI) displayed the presence of not only absorption peaks of rGO at 272 nm (the excitation of π-plasmon of the graphitic structure)[69] but also CeO_2@TiO_2 and TiO_2@CeO_2 absorption around 320−350 nm, indicating the existence of rGO and core−shell nanospheres. Such diversity in absorption features of applied ternary nanocomposites indicated that core−shell nanospheres were successfully located in rGO sheets. The reduction in the ternary nanocomposites absorption peak intensity proved the effective application of the created electron−hole pairs via the carbon substrate and core−shell nanospheres. Furthermore, by using the Tauc plot method, the optical band gap energies were measured. Figure 8b showed the results and the Tauc equation as follows (eq 3):

$$(\alpha h\nu) = \beta(h\nu - E_g)^n \quad (3)$$

where $h\nu$ is the identical photon energy (eV), α represents the absorption coefficient, β shows a proportionality constant, E_g presents the band gap (eV) of the sample substance, while n is an exponent that gets values of 1/2 and 2 based on the nature of electronic transition. For measuring direct band gap replacement was $n = 1/2$ and also for indirect band gap was $n = 2$. After the replacement $n = 1/2$, the Tauc formula for direct band gap will be as presented in eq 4.

$$(\alpha h\nu)^2 = \beta(h\nu - E_g) \quad (4)$$

The curve of the graph was depicted as $(\alpha h\nu)^2$ versus $h\nu$. Thus, for determining the band gap, we fit the data absorption to the direct transition equation using extrapolating the linear part of the curve to absorption that is equal to zero.[70] Therefore, the energy band gaps of TiO_2, CeO_2, CeO_2@TiO_2, TiO_2@CeO_2, rGO-CeO_2@TiO_2, and rGO-TiO_2@CeO_2 were identified to be 3.15, 2.74, 2.42, 2.65, 2.03, and 2.2 eV, respectively (Figure 8b). The measured values of band gap nanoparticles and core−shell nanospheres could be compared with previous research studies.[40,56] It is distinct that the band gap energy of the core−shell nanospheres reduced after it was coated. The obtained results demonstrated that after forming core−shell nanospheres the value of band gap decreases gradually and hence, results in photocatalytic degradation of RhB dye under UV light irradiation. As is shown, the optical consequences depict the reduction of the band gap of the ternary nanocomposites in comparison with core−shell nanospheres, which was because of its higher application efficiency of UV light as compared with TiO_2, CeO_2, TiO_2@CeO_2, and CeO_2@TiO_2. The study of the energy plot of rGO-CeO_2@TiO_2, as well as rGO-TiO_2@CeO_2, reveals that rGO has the main role in improving the effective electron transfer from the bandgap of core−shells to the rGO surface. Thus, this confirmed the higher optical features of ternary nanocomposites that lead to enhanced photocatalytic performance.

3.3. Photocatalytic Degradation Performance. The photocatalytic performance of the prepared photocatalysts was achieved by the determination of the degradation rate of RhB under UV light irradiation. The effective conditions for the degradation process, such as solution pH, catalyst dosage, time, and temperature, were optimized by applying TiO_2 nanoparticles as a control sample.

3.3.1. Effect of Photocatalyst Concentration. The photocatalyst amount effect on RhB degradation was investigated by

https://doi.org/10.1021/acsomega.2c04338
ACS Omega 2022, 7, 30601−30621

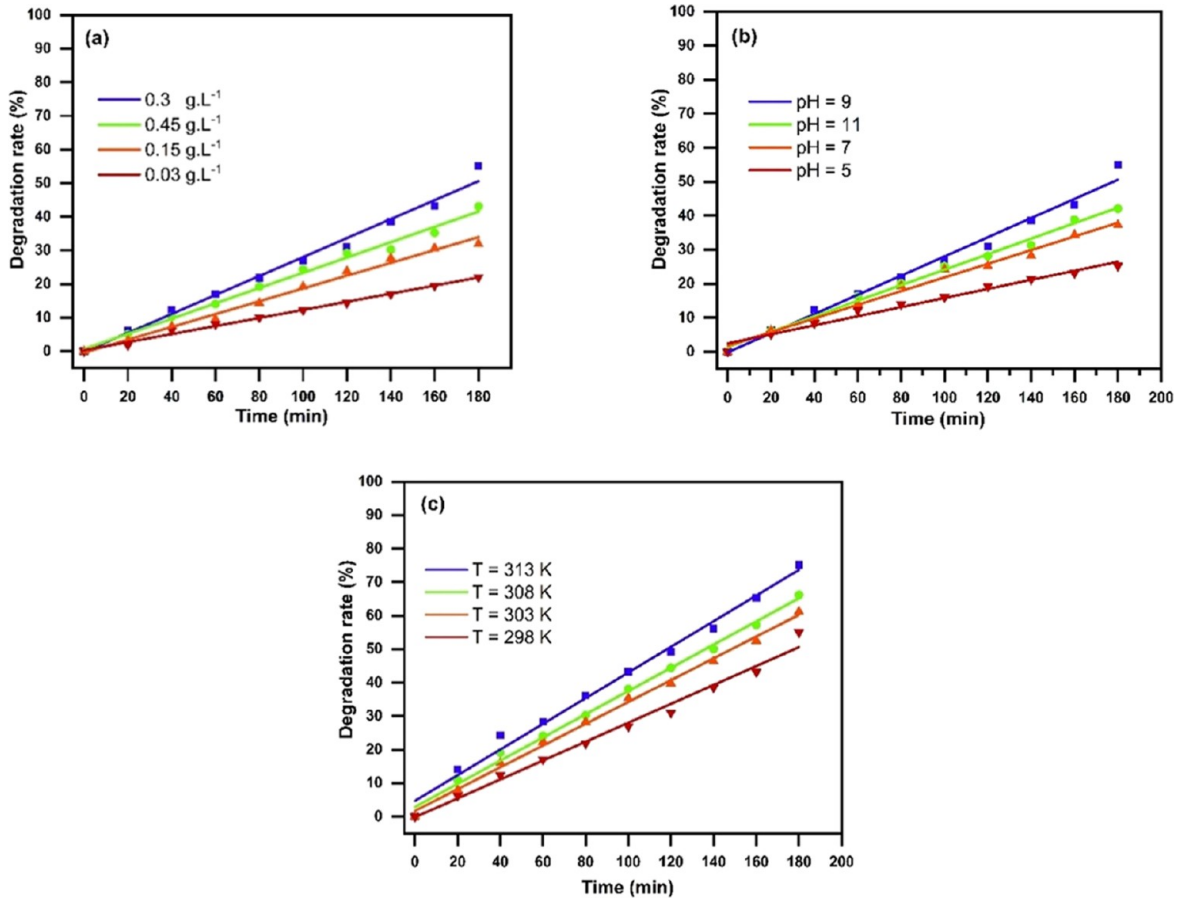

Figure 9. Rate of RhB degradation in the presence of TiO_2 under (a) different concentrations of catalyst, (b) range of pH, and (c) different temperatures.

altering the mass concentration of initial TiO_2 in the range of 0.03−0.45 g L^{-1} for 100 mL of RhB dye with 3 mg L^{-1} concentration at the pH = 9, while the contact duration was 180 min. The degradation curves of RhB with different dosages of TiO_2 are presented in Figure 9a while using UV light. The degradation rate reached 22% within 180 min when the amount of TiO_2 was 0.03 g L^{-1}. Increasing the photocatalyst amount from 0.03 to 0.3 g L^{-1} resulted in the increase of active sites on the photocatalyst and then enhanced the degradation effectiveness of RhB, which reached 55% after 180 min treatment at the maximum, while the amount of the catalyst was 0.3 g L^{-1}. This result also originated from the increase of the number of photons and dye molecules that were absorbed on the surface of the photocatalyst, which is in turn resulted in a combination interaction of the efficient surface area and light diffusing of the catalyst.[71] The more enhancements in the amount of the catalyst to 0.45 g L^{-1} had a negative impact on the degradation effect of RhB. High concentration of catalysts caused an increase in the light scattering and reduced light penetration due to the agglomeration. Therefore, $OH^{\cdot}$ radicals as the first oxidants in the photocatalytic system were reduced, and subsequently, the degradation effect of RhB increased.[72] Then, 0.3 g L^{-1} of catalyst was the most suitable amount and was applied for the future experiments.

3.3.2. Effect of pH. pH plays a crucial role in treating wastewater because it greatly affects hydroxyl radicals' production, particularly in the dye degradation. Thus, RhB decolorization was performed in the range of pH 5 to 11. The test was conducted with 0.3 g L^{-1} of TiO_2 NPs as well as the 100 mL dye concentration of 3 mg L^{-1} under UV light irradiation. For preparation of alkaline and acidic environments, the 0.1 M NaOH and HCl solutions were used, and every dish was put on a hotplate stirrer for 180 min at ambient temperature. In the TiO_2 system under UV illumination, the degradation amount of the RhB dye at alkaline pH values was greater than twofold enhancement when pH enhanced from 5 to 9. The maximum degradation rate was obtained at pH 9 (Figure 9b). While the pH values gradually increased, the photodegradation rate of the organic dye was also increased. The obtained results were obviously coordinated with the electrostatic interaction between the RhB dye and the surface of the photocatalyst, based on the pH of the suspension.[71] In general, the impact of the pH value on the photocatalytic activity is ascribed to the surface absorption of the catalyst and its connection with the ionic form of the organic mixture (anion or cation) between the catalyst surface and the organic molecules and regarding electrostatic attraction or repulsion the photodegradation enhances or inhibits, respectively. However, RhB dye is an ionizable compound, so the enhancement of the reaction value at alkaline pH could be attributed to the high hydroxylation of the photocatalyst surface because of the existence of a great amount of OH^{-} ions. At the alkaline pH (pH > 9), the electrostatic adsorption was optimized, and the hydroxyl groups on the catalyst surface reduced at the same time. This results in the decrease of the photodegradation value at pH > 9. Therefore, an optimal pH value of 9 was selected for the photocatalytic activity of RhB on the TiO_2 catalyst surface.[71] Moreover, it is noteworthy that under acidic pH conditions, dye removal

https://doi.org/10.1021/acsomega.2c04338
ACS Omega 2022, 7, 30601−30621

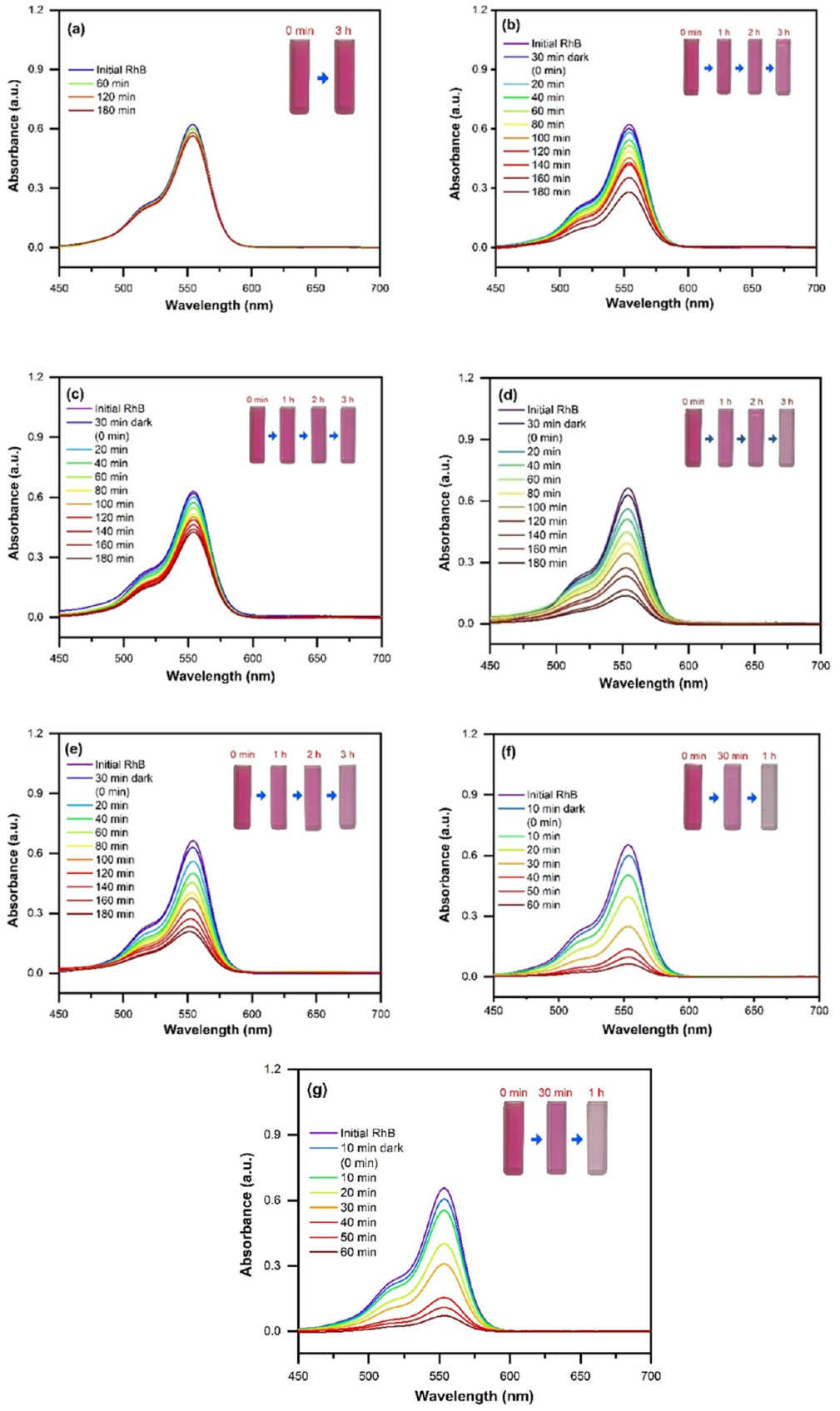

Figure 10. UV−Vis spectra for RhB dye adsorption: (a) without catalyst for 180 min, (b) CeO_2 nanoparticles for 180 min, (c) TiO_2 nanoparticles for 180 min, (d) CeO_2@TiO_2 core−shell nanosphere for 180 min, (e) TiO_2@CeO_2 core−shell nanosphere for 180 min, (f) rGO-CeO_2@TiO_2 ternary nanocomposite for 60 min, and (g) rGO-TiO_2@CeO_2 ternary nanocomposite for 60 min.

https://doi.org/10.1021/acsomega.2c04338
ACS Omega 2022, 7, 30601−30621

decreases considerably because titanium oxide nanoparticles react with hydrogen ion and lose their oxygen and being water-soluble in water (eq 5), and subsequently lose their photocatalyst characteristic.[73]

$$TiO_{2(s)} + 2H^{+}_{(g)} \rightarrow Ti^{4+}_{(aq)} + H_2O_{(L)} \quad (5)$$

3.3.3. Temperature Effect on the RhB Degradation. As represented in Figure 9c, the effect of temperature on the degradation rate of TiO_2 nanoparticles was investigated. A 100 mL solution containing RhB dye was prepared under the optimal conditions involving a catalyst dosage of 0.3 g L^{-1} and pH = 9 and. The prepared solutions were incubated at temperatures of 298, 303, 308, and 313 K and then exposed by UV light for 180 min at 20 min intervals. Then, the effectiveness of photodegradation was calculated according to obtained results. Obviously, temperature creates a powerful effect on the degradation rate of TiO_2 nanoparticles while the temperature enhanced. The degradation rate increased from 55% at 298 K to 75.20% at 313 K, due to the significant effect of increased temperature on the quantity of RhB removal from the solution and the observed activity presumed as an endothermic procedure. The observed dye removal rate was enhanced after addition of the TiO_2 photocatalyst and temperature increase, which may originate from faster molecule movement, which results in the increase of the efficient collision between RhB and TiO_2 nanoparticles. Therefore, it enhances the feasibility of molecules of dyes on the photocatalyst substrate. Also, more free radicals and bubble formation will occur in dye solution at higher temperatures. Finally, the rate of electron−hole pair recombination decreases at the high temperature, and therefore, it causes the increase in dye degradation of the photocatalyst more effectively. Thus, after optimization 298 K was exploited as the optimal temperature in this experiment.

3.3.4. Photocatalytic Measurement and Analysis. The photocatalytic activity of functional nanostructures was determined through obtained optimized factors. Figure 10a−g represents the degradation curves of RhB solution degradation by adding catalyst samples including (a) without catalyst, (b) CeO_2, (c) TiO_2, (d) CeO_2@TiO_2, (e) TiO_2@CeO_2, (f) rGO-CeO_2@TiO_2, and (g) rGO-TiO_2@CeO_2 under the optimal conditions. In this research, CeO_2 and TiO_2 nanoparticles and TiO_2@CeO_2 and CeO_2@TiO_2 core−shell nanospheres were constantly stirred for around 30 min in darkness to achieve the stability of adsorption−desorption equilibrium before irradiation. Afterward, the entire solution that involved the dispersed sample was located under UV light irradiation. UV light irradiation led to more electron excitation and photogenerated holes in the VB and electrons in the CB of applied ternary nanocomposite constituents. This process produces plenty of powerful free radicals, which could decompose the RhB dye more efficiently. As the consequences attained displayed in Figure 10, the photocatalytic function of rGO-CeO_2@TiO_2, as well as rGO-TiO_2@CeO_2 ternary nanocomposites, is much more optimized than that of the other samples, which makes them efficient for the degradation of RhB. In Figure 10a, the blank experiment without a photocatalyst was researched for comparison as well. We observed that the lack of the photocatalyst resulted in degradation in the darkness conditions, and ∼3.21, 1.7, 5.3, and 5.1% of the initial dye were removed from the aqueous solutions that contain CeO_2, TiO_2, CeO_2@TiO_2, and TiO_2@CeO_2 in 30 min, respectively. In addition, about 2% of the initial dye was removed from rGO-CeO_2@TiO_2, and rGO-TiO_2@CeO_2 solution during 10 min. The photocatalytic degradation curves of nanoparticles, core−shell nanospheres and ternary nanocomposites were compared to determine their efficiencies. As illustrated in Figure 10b,c, CeO_2 and TiO_2 nanoparticles could degrade 53.43 and 31.45% of RhB dye molecules while exposed under UV light irradiation for 180 min, respectively. It is noteworthy that the effectiveness of RhB degradation by CeO_2 and TiO_2 is approximately lower under UV light irradiation, which is due to its wide band gap with low performance under UV light.[40] Thus, for CeO_2 nanocubes and TiO_2, the dye adsorption peak at about 554 nm has a little reduction in strength with no hypochromic shift even after being irradiated for 180 min. Hence, Figure 10d,e obviously shows that when the CeO_2@TiO_2 and TiO_2@CeO_2 core−shell nanospheres existed in the RhB solution, the reduction of intensity of the 554 nm peak is more than that for the solution containing CeO_2 nanocubes and TiO_2. The reduction of absorbance is caused by the split of the conjugated chromophore structure.[56] Therefore, cerium dioxide (CeO_2) and titanium dioxide (TiO_2) are assumed to be a proper material in combination form due to their thin band gap and the Ce^{4+}/Ce^{3+} reversible redox couple.[2] According to Chen et al., the RhB dye degradation occurred using the CeO_2/TiO_2 nanocomposite.[56] In the presence of the CeO_2/TiO_2 nanocomposite in the RhB solution, the reduction of the 554 nm peak was higher than the intensity of solutions having CeO_2 nanocubes and TiO_2. Therefore, it is assumed that combining CeO_2 and TiO_2 creates a core−shell structure, which facilitates an optimized UV light degradation reaction of CeO_2/TiO_2 in comparison with those of CeO_2 nanocubes and TiO_2. Figure 10d,e shows the CeO_2@TiO_2 and TiO_2@CeO_2 core−shell nanosphere degradation rate around 78.37 and 67.46% under irradiation by UV light for 180 min, respectively. Ultimately, it was seen that the rGO-CeO_2@TiO_2 and rGO-TiO_2@CeO_2 ternary nanocomposites possess much greater photocatalytic degradation impact on RhB compared to other samples (Figure 10f,g). The obtained results showed 90.35 and 88.2% RhB dye degradation after being exposed to UV light irradiation for 60 min that affirmed the accumulative effect of rGO content on the photocatalytic reaction. The results displayed that the appropriate band gap and interfacial structure of ternary nanocomposites played an effective role in enhancing the photocatalytic activity, which stimulates the greatly effective disintegration of photogenerated holes and photoinduced interfacial charge transfer. Additionally, it was concluded that graphene is the convenient electron acceptor and transporter because it has two-dimensions also a p-conjugation structure.[46] The rGO presence optimizes the electron transport that is transferred from the sensitizer to core−shell nanospheres. Furthermore, rGO can decrease the recombination process of the photogenerated charge carrier. Both the sensitizer and rGO developed the photoactivity of core−shell nanospheres to the UV light and make electrical transport more efficiently that, in turn, increases the rates of photodegradation.[62] Wen et al. reported the RhB dye degradation using the CeO_2−TiO_2−rGO composite.[74] They illustrated that the ternary system effect of the CeO_2−TiO_2−rGO composite photocatalyst enhanced the photocatalytic degradation of RhB organic solution compared with the binary system of the CeO_2−TiO_2 or TiO_2−rGO composite photocatalyst. Figure 10f,g shows that when the ternary nanocomposite was applied as a photocatalyst, the violet color of the activity solution changes into a colorless solution. Consequently, the ternary nanocomposite (rGO-CeO_2@TiO_2 and rGO-TiO_2@CeO_2) photocatalysts irradiated with light

https://doi.org/10.1021/acsomega.2c04338
ACS Omega 2022, 7, 30601−30621

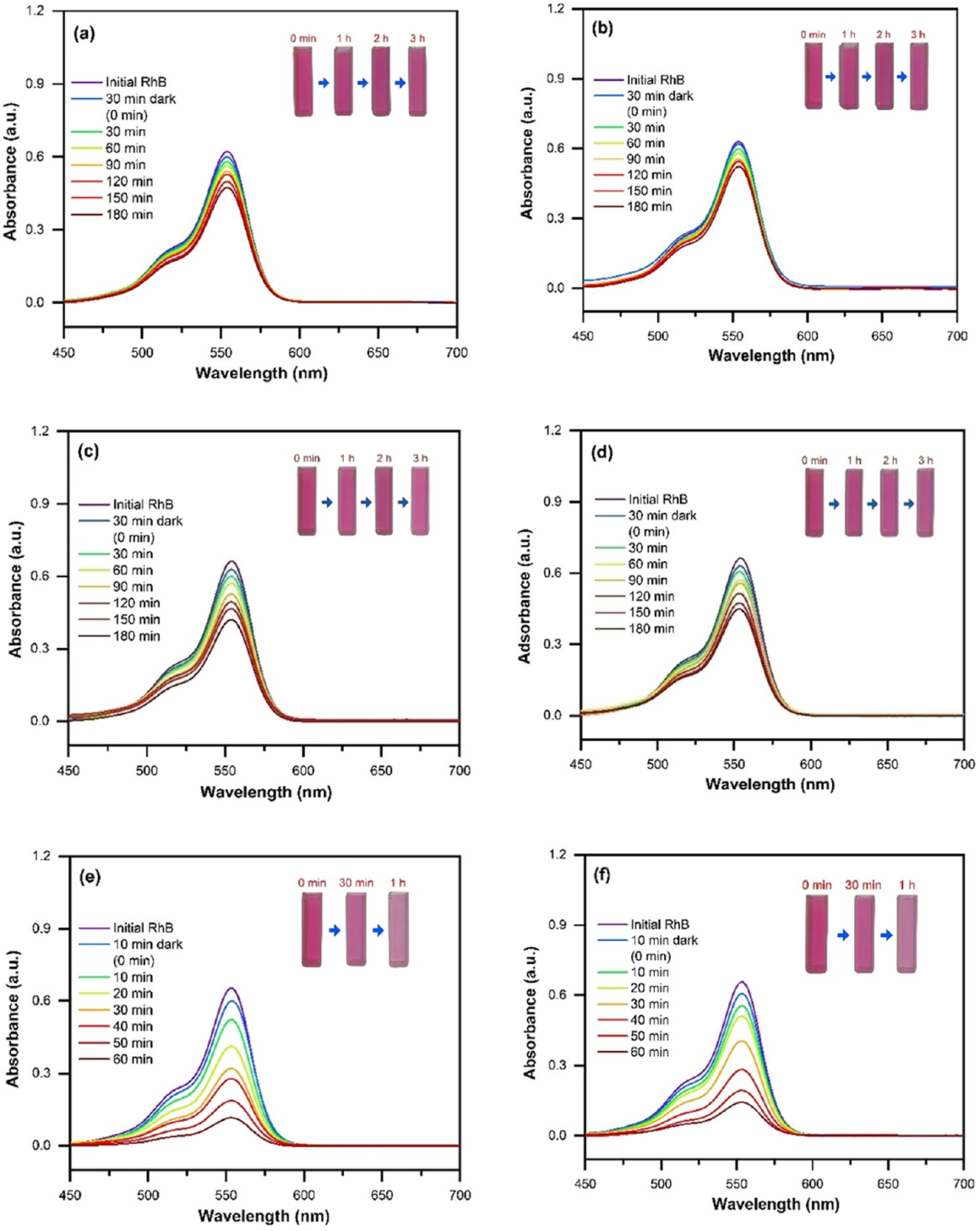

Figure 11. UV−Vis spectra for RhB dye adsorption: (a) CeO_2 nanoparticles for 180 min, (b) TiO_2 nanoparticles for 180 min, (c) CeO_2@TiO_2 core−shell nanospheres for 180 min, (d) TiO_2@CeO_2 core−shell nanospheres for 180 min, (e) rGO-CeO_2@TiO_2 ternary nanocomposites for 60 min, and (f) rGO-TiO_2@CeO_2 ternary nanocomposites for 60 min.

photons. The photogenerated electrons from the VB) electrons to CB are caught by the rGO sheets using a semiconductor carbon heterojunction. At the same time, an equal number of holes have been formed in semiconductor core−shell nanospheres. The electrons are received from the CB of semiconductors by rGO sheets. This procedure greatly increased photogenerated charge separation effectively. These scattered electrons and holes reacted with oxygen and OH directly to create highly reactive radicals of $O_2^{\cdot}$ and $OH^{\cdot}$.[45] Table S1 represents the photocatalytic reaction of all used samples.

3.3.5. Adsorption Activity of RhB. For determination of the nanostructure adsorption value, the adsorption of RhB was determined by the CeO_2 and TiO_2 NPs, TiO_2@CeO_2, and CeO_2@TiO_2 core−shell nanospheres as well as rGO-CeO_2@TiO_2 and rGO-TiO_2@CeO_2 ternary nanocomposites under the optimal conditions (Figure 11a−f). To investigate the appropriate exposure time, the adsorption rate of RhB was

https://doi.org/10.1021/acsomega.2c04338
ACS Omega 2022, 7, 30601−30621

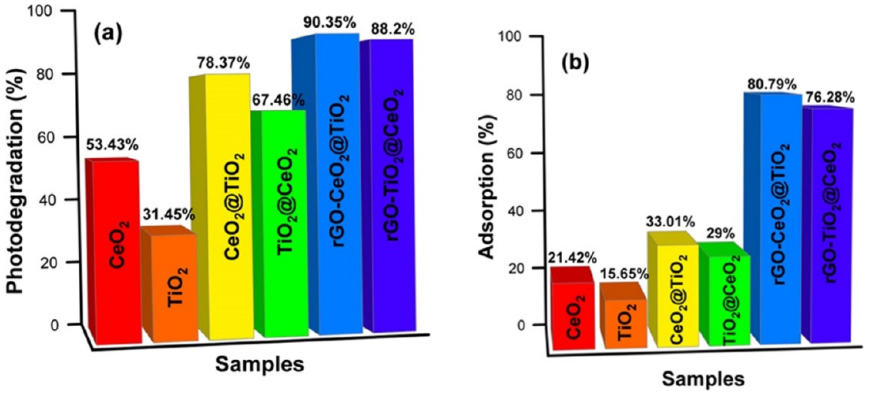

Figure 12. (a) Photodegradation of RhB under UV−Vis irradiation by CeO_2 nanoparticles, TiO_2 nanoparticles, CeO_2@TiO_2 core−shell nanospheres, TiO_2@CeO_2 core−shell nanospheres, rGO-CeO_2@TiO_2 ternary nanocomposites, and rGO-TiO_2@CeO_2 ternary nanocomposites. (b) Comparison of RhB dye adsorption by CeO_2 nanoparticles, TiO_2 nanoparticles, CeO_2@TiO_2 core−shell nanospheres, TiO_2@CeO_2 core−shell nanospheres, rGO-CeO_2@TiO_2 ternary nanocomposites and, rGO-TiO_2@CeO_2 ternary nanocomposites.

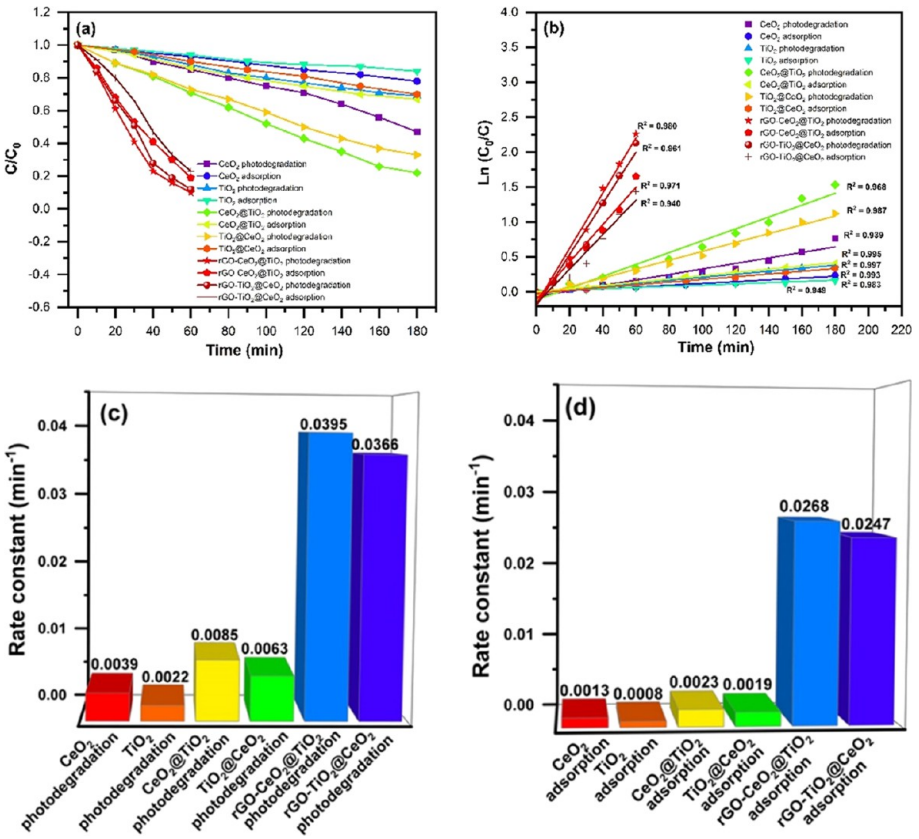

Figure 13. (a) Photodegradation and adsorption kinetics of RhB by the applied synthesized samples under UV light and dark conditions, (b) photodegradation and adsorption kinetic analysis of RhB by different samples, (c) photodegradation rate of RhB degradation by synthesized samples under UV light, and (d) adsorption rate of RhB by synthesized samples under dark conditions.

determined under dark conditions to measure the pure adsorption. Obviously, the CeO_2 and TiO_2 NPs indicated 21.42 and 15.65% as well as CeO_2@TiO_2 and TiO_2@CeO_2 core−shell nanospheres exhibited 33.01 and 29% of RhB dye molecules adsorption in 180 min, respectively. The amounts of adsorption of CeO_2@TiO_2 and TiO_2@CeO_2 core−shell nanospheres were optimized after using rGO considerably. Additionally, rGO-CeO_2@TiO_2 and rGO-TiO_2@CeO_2 ternary nanocomposites could absorb 80.79 and 76.28% of RhB dye during 30 min. Therefore, the RhB adsorption values were as follows: rGO-CeO_2@TiO_2 > rGO-TiO_2@CeO_2 > CeO_2@TiO_2 > TiO_2@CeO_2 > CeO_2 > TiO_2.

As presented in Table 3, it was concluded that reduction of pore sizes enhanced the pore number and also increased the entire volume of pores that finally created more surface area for RhB adsorption. Table S2 represents the adsorption reaction of the samples. The data showed the trend of reduction in RhB adsorption after contact time increase because the RhB filled the pores. The comparison between RhB degradation and RhB adsorption is illustrated in Figure 12a,b using the as-prepared samples. In comparison, the photocatalytic degradation in rGO-

https://doi.org/10.1021/acsomega.2c04338
ACS Omega 2022, 7, 30601−30621

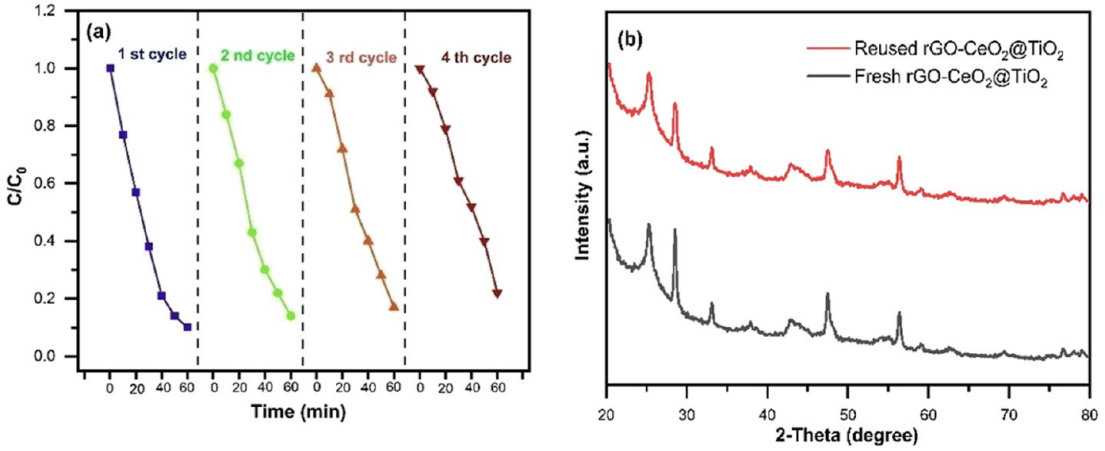

Figure 14. Stability test of (a) reuse experiments of rGO-CeO_2@TiO_2 ternary nanocomposite for RhB photocatalytic degradation. (b) XRD analysis of the rGO-CeO_2@TiO_2 ternary nanocomposite before and after four consecutive recycling photocatalysis.

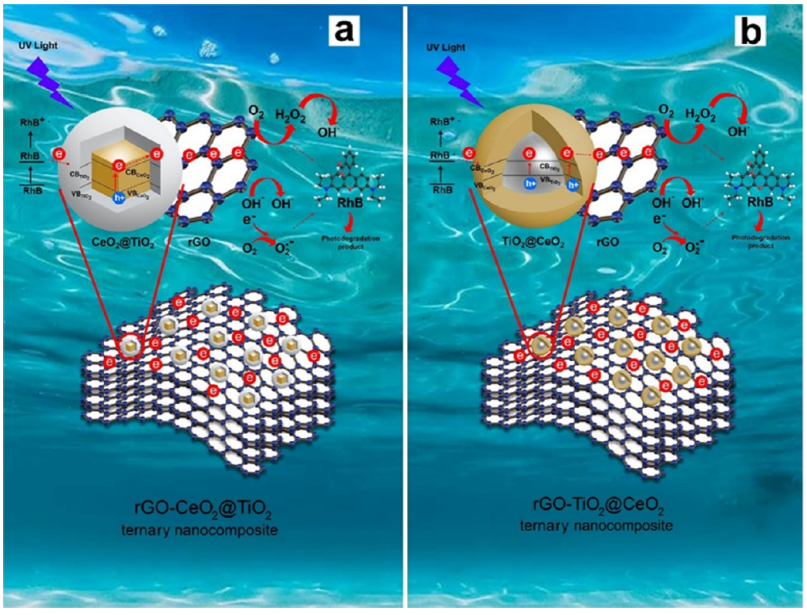

Figure 15. (a) Proposed mechanism of RhB degradation through electron transfer in the rGO-CeO_2@TiO_2 ternary nanocomposite, and (b) proposed mechanism of RhB degradation through electron transfer in the rGO-TiO_2@CeO_2 ternary nanocomposite.

CeO_2@TiO_2 was superior to that of other samples that could nearly degrade 90.35% of the RhB dye in an aqueous solution. Thus, we concluded that the efficiency of the photocatalytic reaction could be enhanced by increasing the contact surface of the photocatalyst with target pollutants to be readily react with the short-lived OH• free radicals and to serve as scavengers for generated e^- and h^+.

3.3.6. Kinetics of Applied Reaction. The RhB dye concentration (C/C_0) was determined using CeO_2 and TiO_2 NPs, CeO_2@TiO_2 and TiO_2@CeO_2 core−shell nanospheres, and rGO-CeO_2@TiO_2 and rGO-TiO_2@CeO_2 ternary nanocomposites under UV light and darkness conditions to display the adsorption kinetic and photodegradation activities, respectively. Figure 13a shows that the rGO-CeO_2@TiO_2 ternary nanocomposite demonstrated the best photocatalytic activity compared with other samples. The degradation efficiency of RhB was in the following order: rGO-CeO_2@TiO_2 > rGO-TiO_2@CeO_2 > CeO_2@TiO_2 > TiO_2@CeO_2 > CeO_2 > TiO_2 and RhB adsorption effectiveness in darkness was also follows: rGO-CeO_2@TiO_2 > rGO-TiO_2@CeO_2 > CeO_2@TiO_2 > TiO_2@CeO_2 > CeO_2 > TiO_2. The pseudo-first-order of kinetic models were used to investigate the kinetics of RhB adsorption and photodegradation by eq 6 as follows:

$$\ln\left(\frac{C_0}{C}\right) = kt \tag{6}$$

where t and k show time and the photodegradation constant rate, respectively, and were calculated in accordance with the patterns of $\ln(C_0/C)$ vs time. The constant rate values are displayed in Figure 13b−d. The rGO-CeO_2@TiO_2 and rGO-TiO_2@CeO_2 ternary nanocomposite photodegradation had a most superior rate constant value of 0.0395 and 0.0366 min^{-1} compared with rGO-CeO_2@TiO_2 and rGO-TiO_2@CeO_2 ternary nanocomposite adsorption of 0.0268 and 0.0247 min^{-1}, CeO_2@TiO_2 and rGO-TiO_2@CeO_2 core−shell nanosphere photodegradation of 0.0085 and 0.0063 min^{-1}, CeO_2@TiO_2 and TiO_2@CeO_2 core−shell nanosphere adsorption of 0.0023 and 0.0019 min^{-1}, CeO_2 and TiO_2 nanoparticle photodegradation of 0.0039 and 0.0022 min^{-1}, and CeO_2 and

https://doi.org/10.1021/acsomega.2c04338
ACS Omega 2022, 7, 30601−30621

TiO_2 nanoparticle adsorption 0.0013 and 0.0008 min^{-1}. Therefore, the photocatalytic performance of rGO-CeO_2@TiO_2 was much more effective than that of the other samples. In addition, the obtained constant rate values showed that all prepared nanostructures had more adsorption efficiency under UV light irradiation than in darkness and also, the RhB dye degradation was faster and in greater amount under UV light.

3.4. Reusability and Stability of the rGO-CeO_2@TiO_2 Ternary Nanocomposite. Stability and reusability are crucial factors for the photocatalytic reaction because the high constancy of the catalyst is important in industry's economies. Figure 14a represents the reusability of the rGO-CeO_2@TiO_2 ternary nanocomposite for RhB photodegradation. It was investigated over four cycles at UV light irradiation, and the concentration of dye was adjusted every time to its initial rate. The photocatalyst/dye molecules were collected after each experiment and rinsed with deionized water, to reuse them in the next cycle under identical test conditions. Photocatalysts were reapplied for four cycles and the degradation values were attained as follows: 90.35, 86.24, 82.87, and 77.83%. Of course, the effectiveness of the rGO-CeO_2@TiO_2 ternary nanocomposite did not reduce considerably, which showed that the catalyst constancy and sustainability were quite suitable for practical application in purifying the environmental contaminants. The XRD plots of the rGO-CeO_2@TiO_2 are displayed in Figure 14b after four runs. It could be apparently observed that the structure and phase of rGO-CeO_2@TiO_2 remained identical and showed that rGO-CeO_2@TiO_2 had a perfect stability for RhB photocatalytic degradation.

3.5. Photocatalytic Mechanism. To understand the enhanced photocatalytic function of rGO-CeO_2@TiO_2 and rGO-TiO_2@CeO_2 ternary nanocomposites, the proposed mechanism is shown in Figure 15a, It was suggested that the mechanism is on the basis of electron−hole induction as well as electron transfer under UV light irradiation. The procedure of charge transfer from nanocomposites toward dye caused dye degradation. During dye treatment with UV light illumination, electrons were stimulated from the VB into CB, and thus the separation of electron−hole pairs occurred. The holes in the VB and the electrons in the CB reacted indirectly or directly with molecules of water and oxygen and created $OH^{\cdot}$ radicals and peroxide, respectively. The degradation procedure of various organic dyes was performed under UV light illumination and was dependent on the oxidation of active oxygen functional groups. The generated free radicals resulted in the degradation reaction and then converted the organic pollutants into CO_2 and H_2O as well as inorganic anions. Previously, many ternary nanocomposites have been considered as suitable photocatalysts.[48] Figure 15a suggests and illustrates a feasible model concerning the photocatalytic activity of CeO_2@TiO_2 under UV light irradiation. Deposition of the TiO_2 shell around CeO_2 nanocubes created a heterojunction structure that increased photoinduced charge separation. CeO_2 could be incited when exposed to UV light, which results in creation of holes in the VB and migration of electrons to the CB. During the photocatalytic process, the excited electrons in the CB of CeO_2 transfer to the CB of TiO_2 due to its more negative CB energy than that of CeO_2.[40] These electrons reduce the surface-adsorbed O_2 on TiO_2 and then generate the perhydroxyl radical ($OOH^{\cdot}$) and superoxide radical anion ($O_2^{\cdot-}$), and generated radicals can react to produce hydroxyl radical ($OH^{\cdot}$),[56] and their degradation activity results in *N*-deethylation of RhB. The CeO_2 holes oxidized the surface-adsorbed OH^- or H_2O in order to produce $OH^{\cdot}$ that had a similar role to the above-generated $OH^{\cdot}$ on TiO_2. Nonetheless, both CeO_2 and TiO_2, after exposing in the light with $\lambda > 470$ nm, were not excitable, and the RhB is the sole light absorbing kind that was incited to the dye-excited mode (RhB*). In addition, the excited electron by RhB* transfers to the CB of TiO_2 and then changes to the radical cation ($RhB^{\cdot+}$).[56] Thus, in the CeO_2@TiO_2 core−shell structure under UV light irradiation, electrons (e^-) are simulated from the VB to the CB of the TiO_2 shell, making holes (h^+) in the VB. In the absence of rGO, numerous charges quickly recombine and result in a low photocatalytic reaction. However in the ternary nanocomposite, the CeO_2@TiO_2 core−shell nanospheres are in close contact with rGO that can create a synergic effect.[46] The rGO serves as an electron acceptor as well as the transporter to separate the photogenerated electron−hole pairs efficiently and prevent the recombination of photogenerated electron−hole pairs. This process led to participation of most holes in the photoinduced oxidation procedure and enhancement of the photocatalytic reaction. On the other hand, the plot mechanism of photocatalytic activity for the rGO-TiO_2@CeO_2 ternary nanocomposite is presented in Figure 15b. At the first step, UV light can incite both CeO_2 and TiO_2 that result in generation of photogenerated holes (h^+) in the VB and electrons (e^-) in their CB.[40] The e^- in the CB of CeO_2 transfers to the rGO easily. In the TiO_2@CeO_2 core−shell nanospheres, the TiO_2 core that is wrapped by the CeO_2 shell has low access to oxygen, OH or surface-absorbed water molecules. Thus, the created electron−hole pairs are combined again in the TiO_2 core. The recombination rate is reduced via adding rGO due to efficient separation of electron and hole pairs. Basically, this is on the basis of perfect conductive and absorption abilities of rGO layers. However, the existence of TiO_2@CeO_2 core−shell nanospheres on the rGO substrate inhibits the stacking of rGO layers and enhances the entire effective surface area considerably in order to absorb and ruin organic pollutants from the water solution. Thus, ternary nanocomposites displayed a higher degradation percentage compared with the TiO_2@CeO_2 core−shell nanospheres.[67] Therefore, according to the above photocatalytic degradation study, the proposed possible mechanism is briefly explained as follows (eqs 789101112):

$$\text{rGO} - \text{CeO}_2@\text{TiO}_2 + h\nu \rightarrow \text{rGO} - \text{CeO}_2@\text{TiO}_2(e^-_{CB} + h^+_{VB}) \quad (7)$$

$$\text{rGO} - \text{TiO}_2@\text{CeO}_2 + h\nu \rightarrow \text{rGO} - \text{TiO}_2@\text{CeO}_2 \quad (8)$$

$$e^- + O_2 \rightarrow O_2^{\cdot-} \quad (9)$$

$$O_2^{\cdot-} + H_2O \rightarrow OH_2^- + OH^- \quad (10)$$

$$h^+ + OH^- \rightarrow OH^{\cdot} \quad (11)$$

$$OH^{\cdot} + O_2^{\cdot-} \rightarrow CO_2 + H_2O + \text{oxidation products} \quad (12)$$

If the present charge carrier pairs (e^-/h^+) not scavenged on the ternary composite surface by water molecules or trapped within the photocatalyst defect sites. They may recombine and result in photonic efficiency and compromise the $OH^{\bullet}$ radical production and inhibit the dye photodegradation. Also, it has been demonstrated that the recombination timescale of e^- and h^+ is in the order of nanoseconds.[75] Therefore, it is critical to provide adequate scavengers for these charge carriers in the aqueous system. As a result, a gradual transfer of electrons in

https://doi.org/10.1021/acsomega.2c04338
ACS Omega 2022, 7, 30601−30621

rGO-CeO_2@TiO_2 and rGO-TiO_2@CeO_2 ternary nanocomposites led to electron charge transfer via their interfaces effectively and so enhance the photocatalytic efficiency. According to the obtained results, the rGO-CeO_2@TiO_2 ternary nanocomposite showed higher photocatalytic performance compared to the ternary rGO-TiO_2@CeO_2 nanocomposite, which was attributed to the abovementioned interpretations.

3.6. Cytotoxicity of the rGO-CeO_2@TiO_2 Ternary Nanocomposite. The toxic effect of the photocatalytic nanocomposite against breast cancer cells (MCF-7) was determined through MTT assay. MCF-7 cells were treated with different concentrations (35, 17.5, 8.75, 4.38, 2.19, and 1.09 mg mL^{-1}) of the rGO-CeO_2@TiO_2 nanocomposite for 24 h. The obtained results are shown in Figure 16, which revealed that

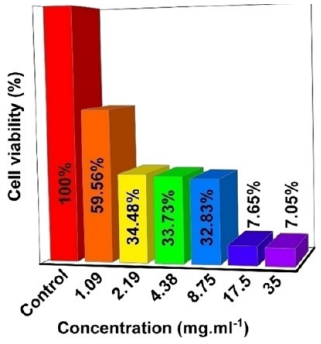

Figure 16. Cytotoxicity of different concentrations (1.09−35 mg mL^{-1}) of the rGO-CeO_2@TiO_2 ternary nanocomposite measured by MTT assay in the MCF7 cell line.

the applied nanocomposite significantly inhibited the proliferation rate of breast cancer cells. The obtained results exhibited dose-dependent potential to induce cell death in MCF-7 cells. The cytotoxicity of the nanocomposite showed a dose-dependent toxic effect with IC50 of about 1 mg mL^{-1}. Highest toxicity (92.35%) was observed in the concentration of 17.5 mg mL^{-1}, which was constant in higher concentration. Hence, the rGO-CeO_2@TiO_2 nanocomposite showed a potent antiproliferation effect on the breast cancer cells. This may be attributed to generation of free radicals by the nanostructure constituents. These free radicals including hydrogen peroxide, superoxide onions, and hydroxyl radicals contribute to serious damage to biological macromolecules such as proteins, carbohydrate, and lipids and also breakage in the cell DNA structure.[76] The accumulation effect of these alterations led to apoptosis of applied cancer cells.

4. CONCLUSIONS

In summary, we have synthesized graphene-based core−shell heterostructure rGO-CeO_2@TiO_2 and rGO-TiO_2@CeO_2 nanocomposites to explore their photocatalytic activity on RhB organic pollutant organic dye. The rGO-CeO_2@TiO_2 ternary nanocomposite showed higher photocatalytic activity because of efficient photogenerated charge carrier separation, reduction of charge recombination, and also a lower band gap value according to the depicted mechanism. MTT assay of the rGO-CeO_2@TiO_2ternary nanocomposite also showed cell cytotoxicity with IC50 of 1 mg mL^{-1}, which illustrated its further biological application.

ASSOCIATED CONTENT

Supporting Information

The Supporting Information is available free of charge at https://pubs.acs.org/doi/10.1021/acsomega.2c04338.

Photocatalytic activity of samples at different times, photocatalytic activity of samples at different times under dark conditions, and particle size distribution of (a) TiO_2 nanoparticles, (b) CeO_2 nanoparticles, (c) CeO_2@TiO_2 core−shell nanospheres, and (d) TiO_2@CeO_2 core−shell nanospheres (PDF)

AUTHOR INFORMATION

Corresponding Author

Fatemeh Ravari − *Department of Chemistry, Payame Noor University, Tehran 193954697, Iran;* orcid.org/0000-0001-8033-6054; Email: fatemeravari@pnu.ac.ir

Authors

Mitra Malekkiani − *Department of Chemistry, Payame Noor University, Tehran 193954697, Iran*

Abbas Heshmati Jannat Magham − *Department of Chemistry, Payame Noor University, Tehran 193954697, Iran*

Mehdi Dadmehr − *Department of Biology, Payame Noor University, Tehran 193954697, Iran*

Heiko Groiss − *Christian Doppler Laboratory for Nanoscale Phase Transformations, Center for Surface and Nanoanalytics, Johannes Kepler University Linz, Linz 4040, Austria*

Hasan Ali Hosseini − *Department of Chemistry, Payame Noor University, Tehran 193954697, Iran*

Reza Sharif − *Christian Doppler Laboratory for Nanoscale Phase Transformations, Center for Surface and Nanoanalytics, Johannes Kepler University Linz, Linz 4040, Austria*

Complete contact information is available at: https://pubs.acs.org/10.1021/acsomega.2c04338

Notes

The authors declare no competing financial interest.

ACKNOWLEDGMENTS

The financial support by the Austrian Federal Ministry for Digital and Economic Affairs, the National Foundation for Research, Technology, and Development, and the Christian Doppler Research Association is gratefully acknowledged. We thank P. Oberhumer (ZONA, JKU Linz) for TEM and STEM-EDS measurements.

REFERENCES

(1) Han, F.; Kambala, V. S. R.; Srinivasan, M.; Rajarathnam, D.; Naidu, R. Tailored titanium dioxide photocatalysts for the degradation of organic dyes in wastewater treatment: a review. *Appl. Catal., A* **2009**, *359*, 25−40.

(2) Mekonnen, T. B. An Overview on the Photocatalytic Degradation of Organic Pollutants in the Presence of Cerium Oxide (CeO_2) Based Nanoparticles: A Review. *Nanosci. nanometrol.* **2021**, *7*, 14.

(3) Naji, A. M.; Mohammed, I. Y.; Mohammed, S. H.; Mohammed, M. K.; Ahmed, D. S.; Jabir, M. S.; Rheima, A. M. Photocatalytic Degradation of Methylene Blue Dye Using F doped ZnO/Polyvinyl Alcohol Nanocomposites. *Mater. Lett.* **2022**, *322*, No. 132473.

(4) Chen, H.; Zhao, J. Adsorption study for removal of Congo red anionic dye using organo-attapulgite. *Adsorption* **2009**, *15*, 381−389.

(5) Huo, S.-H.; Yan, X.-P. Metal−organic framework MIL-100 (Fe) for the adsorption of malachite green from aqueous solution. *J. Mater. Chem.* **2012**, *22*, 7449−7455.

(6) Ong, S.-T.; Keng, P.-S.; Lee, W.-N.; Ha, S.-T.; Hung, Y.-T. Dye waste treatment. *Water* **2011**, *3*, 157−176.
(7) Kornaros, M.; Lyberatos, G. Biological treatment of wastewaters from a dye manufacturing company using a trickling filter. *J. Hazard. Mater.* **2006**, *136*, 95−102.
(8) Anandan, S.; Vinu, A.; Mori, T.; Gokulakrishnan, N.; Srinivasu, P.; Murugesan, V.; Ariga, K. Photocatalytic degradation of 2, 4, 6-trichlorophenol using lanthanum doped ZnO in aqueous suspension. *Catal. Commun.* **2007**, *8*, 1377−1382.
(9) Dong, P.; Wang, Y.; Guo, L.; Liu, B.; Xin, S.; Zhang, J.; Shi, Y.; Zeng, W.; Yin, S. A facile one-step solvothermal synthesis of graphene/rod-shaped TiO_2 nanocomposite and its improved photocatalytic activity. *Nanoscale* **2012**, *4*, 4641−4649.
(10) Moustakas, N.; Katsaros, F.; Kontos, A.; Romanos, G. E.; Dionysiou, D.; Falaras, P. Visible light active TiO_2 photocatalytic filtration membranes with improved permeability and low energy consumption. *Catal. Today* **2014**, *224*, 56−69.
(11) Li, J.-G.; Ishigaki, T.; Sun, X. Anatase, brookite, and rutile nanocrystals via redox reactions under mild hydrothermal conditions: phase-selective synthesis and physicochemical properties. *J. Phys. Chem. C* **2007**, *111*, 4969−4976.
(12) Yu, X.; Huang, L.; Wei, Y.; Zhang, J.; Zhao, Z.; Dai, W.; Yao, B. Controllable preparation, characterization and performance of Cu_2O thin film and photocatalytic degradation of methylene blue using response surface methodology. *Mater. Res. Bull.* **2015**, *64*, 410−417.
(13) Chen, C.; Ma, W.; Zhao, J. Semiconductor-mediated photodegradation of pollutants under visible-light irradiation. *Chem. Soc. Rev.* **2010**, *39*, 4206−4219.
(14) Dolbecq, A.; Mialane, P.; Keita, B.; Nadjo, L. Polyoxometalate-based materials for efficient solar and visible light harvesting: application to the photocatalytic degradation of azo dyes. *J. Mater. Chem.* **2012**, *22*, 24509−24521.
(15) Fan, W.; Zhang, Q.; Wang, Y. Semiconductor-based nanocomposites for photocatalytic H 2 production and CO 2 conversion. *Phys. Chem. Chem. Phys.* **2013**, *15*, 2632−2649.
(16) Kubacka, A.; Fernandez-Garcia, M.; Colon, G. Advanced nanoarchitectures for solar photocatalytic applications. *Chem. Rev.* **2012**, *112*, 1555−1614.
(17) Chen, X.; Shen, S.; Guo, L.; Mao, S. S. Semiconductor-based photocatalytic hydrogen generation. *Chem. Rev.* **2010**, *110*, 6503−6570.
(18) Mo, J.; Zhang, Y.; Xu, Q.; Lamson, J. J.; Zhao, R. Photocatalytic purification of volatile organic compounds in indoor air: A literature review. *Atmos. Environ.* **2009**, *43*, 2229−2246.
(19) Venieri, D.; Gounaki, I.; Binas, V.; Zachopoulos, A.; Kiriakidis, G.; Mantzavinos, D. Inactivation of MS2 coliphage in sewage by solar photocatalysis using metal-doped TiO_2. *Appl. Catal., B* **2015**, *178*, 54−64.
(20) Asaithambi, S.; Sakthivel, P.; Karuppaiah, M.; Yuvakkumar, R.; Balamurugan, K.; Ahamad, T.; Khan, M. M.; Ramalingam, G.; Mohammed, M. K.; Ravi, G. Preparation of Fe-SnO_2@ CeO_2 nanocomposite electrode for asymmetric supercapacitor device performance analysis. *J. Energy Storage* **2021**, *36*, No. 102402.
(21) Mohammed, M. K. Sol-gel synthesis of Au-doped TiO_2 supported SWCNT nanohybrid with visible-light-driven photocatalytic for high degradation performance toward methylene blue dye. *Optik* **2020**, *223*, No. 165607.
(22) Nakata, K.; Fujishima, A. TiO_2 photocatalysis: Design and applications. *J. Photochem. Photobiol., C* **2012**, *13*, 169−189.
(23) Yang, T.-S.; Yang, M.-C.; Shiu, C.-B.; Chang, W.-K.; Wong, M.-S. Effect of N_2 ion flux on the photocatalysis of nitrogen-doped titanium oxide films by electron-beam evaporation. *Appl. Surf. Sci.* **2006**, *252*, 3729−3736.
(24) Yanqing, Z.; Erwei, S.; Zhizhan, C.; Wenjun, L.; Xingfang, H. Influence of solution concentration on the hydrothermal preparation of titania crystallites. *J. Mater. Chem.* **2001**, *11*, 1547−1551.
(25) Binas, V.; Sambani, K.; Maggos, T.; Katsanaki, A.; Kiriakidis, G. Synthesis and photocatalytic activity of Mn-doped TiO_2 nanostructured powders under UV and visible light. *Appl. Catal., B* **2012**, *113*, 79−86.
(26) Chaudhuri, R. G.; Paria, S. Visible light induced photocatalytic activity of sulfur doped hollow TiO_2 nanoparticles, synthesized via a novel route. *Dalton Trans.* **2014**, *43*, 5526−5534.
(27) Yang, M.-H.; Chen, P.-C.; Tsai, M.-C.; Chen, T.-T.; Chang, I.-C.; Chiu, H.-T.; Lee, C.-Y. Alkali metal ion assisted synthesis of faceted anatase TiO_2. *CrystEngComm* **2013**, *15*, 2966−2971.
(28) Dong, Z.; Wu, M.; Wu, J.; Ma, Y.; Ma, Z. In situ synthesis of TiO_2/SnO x−Au ternary heterostructures effectively promoting visible-light photocatalysis. *Dalton Trans.* **2015**, *44*, 11901−11910.
(29) Liu, H.; He, Y.; Liang, X. Magnetic photocatalysts containing TiO_2 nanocrystals: Morphology effect on photocatalytic activity. *J. Mater. Res.* **2014**, *29*, 98−106.
(30) Bessekhouad, Y.; Robert, D.; Weber, J.-V. Photocatalytic activity of Cu_2O/TiO_2, Bi_2O_3/TiO_2 and $ZnMn_2O_4/TiO_2$ heterojunctions. *Catal. Today* **2005**, *101*, 315−321.
(31) Bian, Z.; Zhu, J.; Wang, S.; Cao, Y.; Qian, X.; Li, H. Self-assembly of active Bi_2O_3/TiO_2 visible photocatalyst with ordered mesoporous structure and highly crystallized anatase. *J. Phys. Chem. C* **2008**, *112*, 6258−6262.
(32) Lin, C.-F.; Wu, C.-H.; Onn, Z.-N. Degradation of 4-chlorophenol in TiO_2, WO_3, SnO_2, TiO_2/WO_3 and TiO_2/SnO_2 systems. *J. Hazard. Mater.* **2008**, *154*, 1033−1039.
(33) Mu, J.; Chen, B.; Zhang, M.; Guo, Z.; Zhang, P.; Zhang, Z.; Sun, Y.; Shao, C.; Liu, Y. Enhancement of the visible-light photocatalytic activity of $In_2O_3-TiO_2$ nanofiber heteroarchitectures. *ACS Appl. Mater. Interfaces* **2012**, *4*, 424−430.
(34) Topkaya, E.; Konyar, M.; Yatmaz, H. C.; Öztürk, K. Pure ZnO and composite ZnO/TiO_2 catalyst plates: A comparative study for the degradation of azo dye, pesticide and antibiotic in aqueous solutions. *J. Colloid Interface Sci.* **2014**, *430*, 6−11.
(35) Yang, H.; Zhang, K.; Shi, R.; Tang, A. Sol−gel synthesis and photocatalytic activity of CeO_2/TiO_2 nanocomposites. *J. Am. Ceram. Soc.* **2007**, *90*, 1370−1374.
(36) Zhou, W.; Liu, K.; Fu, H.; Pan, K.; Zhang, L.; Wang, L.; Sun, C.-C. Multi-modal mesoporous TiO_2-ZrO_2 composites with high photocatalytic activity and hydrophilicity. *Nanotechnology* **2007**, *19*, No. 035610.
(37) Asaithambi, S.; Sakthivel, P.; Karuppaiah, M.; Yuvakkumar, R.; Velauthapillai, D.; Ahamad, T.; Khan, M. M.; Mohammed, M. K.; Vijayaprabhu, N.; Ravi, G. The bifunctional performance analysis of synthesized Ce doped SnO_2/g-C3N4 composites for asymmetric supercapacitor and visible light photocatalytic applications. *J. Alloys Compd.* **2021**, *866*, No. 158807.
(38) Guo, X. H.; Mao, C. C.; Zhang, J.; Huang, J.; Wang, W. N.; Deng, Y. H.; Wang, Y. Y.; Cao, Y.; Huang, W. X.; Yu, S. H. Cobalt-Doping-Induced Synthesis of Ceria Nanodisks and Their Significantly Enhanced Catalytic Activity. *Small* **2012**, *8*, 1515−1520.
(39) Qi, J.; Chen, J.; Li, G.; Li, S.; Gao, Y.; Tang, Z. Facile synthesis of core−shell Au@CeO_2 nanocomposites with remarkably enhanced catalytic activity for CO oxidation. *Energy Environ. Sci.* **2012**, *189*, 8937−8941.
(40) Zhang, L.; Zhang, J.; Jiu, H.; Zhang, X.; Xu, M. Preparation of hollow core/shell CeO_2@ TiO_2 with enhanced photocatalytic performance. *J. Mater. Sci.* **2015**, *50*, 5228−5237.
(41) Wang, D.; Han, D.; Yang, J.; Wang, J.; Li, X.; Song, H. Controlled preparation of superparamagnetic Fe_3O_4@ SiO_2@ ZnO-Au core-shell photocatalyst with superior activity: RhB degradation and working mechanism. *Powder Technol.* **2018**, *327*, 489−499.
(42) Li, W.; Yang, J.; Wu, Z.; Wang, J.; Li, B.; Feng, S.; Deng, Y.; Zhang, F.; Zhao, D. A versatile kinetics-controlled coating method to construct uniform porous TiO_2 shells for multifunctional core−shell structures. *J. Am. Chem. Soc.* **2012**, *134* (29), 11864−11867.
(43) Ye, M.; Zhang, Q.; Hu, Y.; Ge, J.; Lu, Z.; He, L.; Chen, Z.; Yin, Y. Magnetically recoverable core−shell nanocomposites with enhanced photocatalytic activity. *Chem. − Eur. J.* **2010**, *16*, 6243−6250.
(44) Wei, X.; Shao, C.; Li, X.; Lu, N.; Wang, K.; Zhang, Z.; Liu, Y. Facile in situ synthesis of plasmonic nanoparticles-decorated gC_3N_4/

https://doi.org/10.1021/acsomega.2c04338
ACS Omega 2022, 7, 30601−30621

TiO_2 heterojunction nanofibers and comparison study of their photosynergistic effects for efficient photocatalytic H_2 evolution. *Nanoscale* **2016**, *8*, 11034−11043.
(45) Thangavel, S.; Thangavel, S.; Raghavan, N.; Krishnamoorthy, K.; Venugopal, G. Visible-light driven photocatalytic degradation of methylene-violet by rGO/Fe_3O_4/ZnO ternary nanohybrid structures. *J. Alloys Compd.* **2016**, *665*, 107−112.
(46) Ma, P.; Jiang, W.; Wang, F.; Li, F.; Shen, P.; Chen, M.; Wang, Y.; Liu, J.; Li, P. Synthesis and photocatalytic property of Fe_3O_4@TiO_2 core/shell nanoparticles supported by reduced graphene oxide sheets. *J. Alloys Compd.* **2013**, *578*, 501−506.
(47) Ishigami, M.; Chen, J.; Cullen, W.; Fuhrer, M.; Williams, E. Atomic structure of graphene on SiO_2. *Nano Lett.* **2007**, *7*, 1643−1648.
(48) Dehghani-Dashtabi, M.; Hekmatara, H.; Seyed-Yazdi, J. Synthesis and improved photoactivity of magnetic quaternary nanocomposites consisting of Fe_3O_4@ ZnO core@ shell nanoparticles decorated on graphene-oxide grafted poly-citric acid. *Phys. B* **2019**, *553*, 11−17.
(49) Dadmehr, M.; Karimi, M. A.; Korouzhdehi, B. A signal-on fluorescence based biosensing platform for highly sensitive detection of DNA methyltransferase enzyme activity and inhibition. *Spectrochim. Acta, Part A* **2020**, *228*, No. 117731.
(50) Karimi, M. A.; Dadmehr, M.; Hosseini, M.; Korouzhdehi, B.; Oroojalian, F. Sensitive detection of methylated DNA and methyltransferase activity based on the lighting up of FAM-labeled DNA quenched fluorescence by gold nanoparticles. *RSC Adv.* **2019**, *9*, 12063−12069.
(51) Mortezaei, M.; Dadmehr, M.; Korouzhdehi, B.; Hakimi, M.; Ramshini, H. Colorimetric and label free detection of gelatinase positive bacteria and gelatinase activity based on aggregation and dissolution of gold nanoparticles. *J. Microbiol. Methods* **2021**, *191*, No. 106349.
(52) Rafiei, S.; Dadmehr, M.; Hosseini, M.; Kermani, H. A.; Ganjali, M. R. A fluorometric study on the effect of DNA methylation on DNA interaction with graphene quantum dots. *Methods Appl. Fluoresc.* **2019**, *7*, No. 025001.
(53) Shahi, S. C.; Dadmehr, M.; Korouzhdehi, B.; Tavassoli, A. A novel colorimetric biosensor for sensitive detection of aflatoxin mediated by bacterial enzymatic reaction in saffron samples. *Nanotechnology* **2021**, *32*, 505503.
(54) Gholami, Z.; Dadmehr, M.; Jelodar, N. B.; Hosseini, M.; Parizi, A. P. One-pot biosynthesis of CdS quantum dots through in vitro regeneration of hairy roots of Rhaphanus sativus L. and their apoptosis effect on MCF-7 and AGS cancerous human cell lines. *Mater. Res. Express* **2020**, *7*, No. 015056.
(55) Wei, X.; Zhu, G.; Fang, J.; Chen, J. Synthesis, characterization, and photocatalysis of well-dispersible phase-pure anatase TiO_2 nanoparticles. *Int. J. Photoenergy* **2013**, *2013*, No. 726872.
(56) Chen, F.; Ho, P.; Ran, R.; Chen, W.; Si, Z.; Wu, X.; Weng, D.; Huang, Z.; Lee, C. Synergistic effect of CeO_2 modified TiO_2 photocatalyst on the enhancement of visible light photocatalytic performance. *J. Alloys Compd.* **2017**, *714*, 560−566.
(57) Noori, M.; Ravari, F.; Ehsani, M. Preparation of PVA nanofibers reinforced with magnetic graphene by electrospinning method and investigation of their degradation kinetics using master plot analyses on solid state. *J. Therm. Anal. Calorim.* **2018**, *132*, 397−406.
(58) Maji, S. K.; Sreejith, S.; Mandal, A. K.; Ma, X.; Zhao, Y. Immobilizing gold nanoparticles in mesoporous silica covered reduced graphene oxide: a hybrid material for cancer cell detection through hydrogen peroxide sensing. *ACS Appl. Mater. Interfaces* **2014**, *6*, 13648−13656.
(59) Akhtar, S.; Shahzad, K.; Mushtaq, S.; Ali, I.; Rafe, M. H.; Fazal-ul-Karim, S. M. Antibacterial and antiviral potential of colloidal Titanium dioxide (TiO_2) nanoparticles suitable for biological applications. *Mater. Res. Express* **2019**, *6*, 105409.
(60) Natarajan, T. S.; Gopi, P. K.; Natarajan, K.; Bajaj, H. C.; Tayade, R. J. TiO_2/graphene oxide nanocomposite with enhanced photocatalytic capacity for degradation of 2, 4-dichlorophenoxyacetic acid herbicide. *Water-Energy Nexus* **2021**, *4*, 103−112.
(61) Murali, A.; Lan, Y.; Sarswat, P.; Free, M. Synthesis of CeO2/reduced graphene oxide nanocomposite for electrochemical determination of ascorbic acid and dopamine and for photocatalytic applications. *Mater. Today Chem.* **2019**, *12*, 222−232.
(62) Vallejo, W.; Rueda, A.; Diaz-Uribe, C.; Grande, C.; Quintana, P. Photocatalytic activity of graphene oxide−TiO_2 thin films sensitized by natural dyes extracted from Bactris guineensis. *R. Soc. Open Sci.* **2019**, *6*, No. 181824.
(63) Manibalan, G.; Murugadoss, G.; Thangamuthu, R.; Kumar, R. M.; Jayavel, R. Facile synthesis of heterostructure CeO_2-TiO_2 nanocomposites for enhanced electrochemical sensor and solar cell applications. *J. Alloys Compd.* **2019**, *773*, 449−461.
(64) Kumar, P.; Som, S.; Pandey, M. K.; Das, S.; Chanda, A.; Singh, J. Investigations on optical properties of ZnO decorated graphene oxide (ZnO@ GO) and reduced graphene oxide (ZnO@ r-GO). *J. Alloys Compd.* **2018**, *744*, 64−74.
(65) Nazari, Y.; Salem, S. Efficient photocatalytic methylene blue degradation by Fe_3O_4@ TiO_2 core/shell linked to graphene by aminopropyltrimethoxysilane. *Environ. Sci. Pollut. Res.* **2019**, *26*, 25359−25371.
(66) Sarigamala, K. K.; Shukla, S.; Struck, A.; Saxena, S. Rationally engineered 3D-dendritic cell-like morphologies of LDH nanostructures using graphene-based core−shell structures. *Microsyst. Nanoeng.* **2019**, *5*, 65.
(67) Cai, J.; Wu, X.; Li, S.; Zheng, F. Controllable location of Au nanoparticles as cocatalyst onto TiO_2@ CeO_2 nanocomposite hollow spheres for enhancing photocatalytic activity. *Appl. Catal., B* **2017**, *201*, 12−21.
(68) Pudukudy, M.; Jia, Q.; Yuan, J.; Megala, S.; Rajendran, R.; Shan, S. Influence of CeO2 loading on the structural, textural, optical and photocatalytic properties of single-pot sol-gel derived ultrafine CeO_2/TiO_2 nanocomposites for the efficient degradation of tetracycline under visible light irradiation. *Mater. Sci. Semicond. Process.* **2020**, *108*, No. 104891.
(69) Dandia, A.; Sharma, A.; Parewa, V.; Kumawat, B.; Rathore, K. S. Amidic C−N bond cleavage of isatin: chemoselective synthesis of pyrrolo [2, 3, 4-kl] acridin-1-ones using Ag NPs decorated rGO composite as an efficient and recoverable catalyst under microwave irradiation. *RSC Adv.* **2015**, *5*, 91888−91902.
(70) Deotale, A. J.; Nandedkar, R. Correlation between particle size, strain and band gap of iron oxide nanoparticles. *Mater. Today: Proc.* **2016**, *3*, 2069−2076.
(71) Kong, J.-Z.; Li, A.-D.; Zhai, H.-F.; Li, H.; Yan, Q.-Y.; Ma, J.; Wu, D. Preparation, characterization and photocatalytic properties of $ZnTiO_3$ powders. *J. Hazard. Mater.* **2009**, *171*, 918−923.
(72) Sun, J.; Wang, X.; Sun, J.; Sun, R.; Sun, S.; Qiao, L. Photocatalytic degradation and kinetics of Orange G using nano-sized Sn (IV)/TiO2/AC photocatalyst. *J. Mol. Catal. A: Chem.* **2006**, *260*, 241−246.
(73) Bagheri, M.; Najafabadi, N. R.; Borna, E. Removal of reactive blue 203 dye photocatalytic using ZnO nanoparticles stabilized on functionalized MWCNTs. *J. King Saud Univ., Sci.* **2020**, *32*, 799−804.
(74) Wen, J.; Hu, G.; Yang, J. Mechanism Research on Photocatalytic Degradation of Organic Waste-water by Ce-Ti-graphene Composite. *IOP Conf. Ser.: Mater. Sci. Eng.* **2018**, *423*, No. 012176.
(75) Liu, B.; Zhao, X.; Zhang, N.; Zhao, Q.; He, X.; Feng, J. Photocatalytic mechanism of TiO2−CeO2 films prepared by magnetron sputtering under UV and visible light. *Surf. Sci.* **2005**, *595*, 203−211.
(76) Sarala, E.; Madhukara Naik, M.; Vinuth, M.; Rami Reddy, Y.; Sujatha, H. Green synthesis of Lawsonia inermis-mediated zinc ferrite nanoparticles for magnetic studies and anticancer activity against breast cancer (MCF-7) cell lines. *J. Mater. Sci.: Mater. Electron.* **2020**, *31*, 8589−8596.

https://doi.org/10.1021/acsomega.2c04338
ACS Omega 2022, 7, 30601−30621